2016

Nitrogen-doped graphene ribbon assembled core-sheath MnO@Graphene scrolls as hierarchically ordered 3D porous electrodes for fast and durable lithium storage

Yun Zhang
Sichuan University, yunz@uow.edu.au

Penghui Chen
Sichuan University

Xu Gao
Sichuan University

Bo Wang
Harbin Institute of Technology

Heng Liu
Sichuan University, h_liu@scu.edu.cn

See next page for additional authors

Publication Details

Zhang, Y., Chen, P., Gao, X., Wang, B., Liu, H., Wu, H., Liu, H. & Dou, S. (2016). Nitrogen-doped graphene ribbon assembled core-sheath MnO@Graphene scrolls as hierarchically ordered 3D porous electrodes for fast and durable lithium storage. Advanced Functional Materials, 26 (43), 7754-7765.

Nitrogen-doped graphene ribbon assembled core-sheath MnO@Graphene scrolls as hierarchically ordered 3D porous electrodes for fast and durable lithium storage

Abstract

Graphene scroll is an emerging 1D tubular form of graphitic carbon that has potential applications in electrochemical energy storage. However, it still remains a challenge to composite graphene scrolls with other nanomaterials for building advanced electrode configuration with fast and durable lithium storage properties. Here, a transition-metal-oxide-based hierarchically ordered 3D porous electrode is designed based on assembling 1D core-sheath MnO@N-doped graphene scrolls with 2D N-doped graphene ribbons. In the resulting architecture, porous MnO nanowires confined in tubular graphene scrolls are mechanically isolated but electronically wellconnected, while the interwoven graphene ribbons offer continuous conductive paths for electron transfer in all directions. Moreover, the elastic graphene scrolls together with enough internal voids are able to accommodate the volume expansion of the enclosed MnO. Because of these merits, the as-built electrode manifests ultrahigh rate capability (349 mAh g−1 at 8.0 A g−1; 205 mAh g−1 at 15.0 A g−1) and robust cycling stability (812 mAh g−1 remaining after 1000 cycles at 2.0 A g−1) and is the most efficient MnO-based anode ever reported for lithium-ion batteries. This unique multidimensional and hierarchically ordered structure design is believed to hold great potential in generalizable synthesis of graphene scrolls composited with oxide nanowires for mutifuctional energy storage.

Keywords

core-sheath, mno@graphene, nitrogen-doped, ordered, 3d, porous, electrodes, fast, durable, graphene, scrolls, hierarchically, lithium, storage, assembled, ribbon

Disciplines

Engineering | Physical Sciences and Mathematics

Publication Details

Zhang, Y., Chen, P., Gao, X., Wang, B., Liu, H., Wu, H., Liu, H. & Dou, S. (2016). Nitrogen-doped graphene ribbon assembled core-sheath MnO@Graphene scrolls as hierarchically ordered 3D porous electrodes for fast and durable lithium storage. Advanced Functional Materials, 26 (43), 7754-7765.

Authors

Yun Zhang, Penghui Chen, Xu Gao, Bo Wang, Heng Liu, Haobin Wu, Hua-Kun Liu, and Shi Xue Dou

PUBLISHED TITLE – "Nitrogen-doped graphene ribbon assembled core-sheath MnO@Graphene scrolls as hierarchically ordered 3D porous electrodes for fast and durable lithium storage"

Engineering 3D Hierarchical Anode Configuration Based on Nitrogen-Doped Graphene–Scrolled MnO Coaxial Nanocables for Superior Lithium Storage

Hao Wu, *Penghui Chen*, *Yi Guo*, *Bo Wang*, *Wenjing Liu*, *Heng Liu*, *Yun Zhang, Shixue Dou, and Huakun Liu*

Keywords: hierarchical structure; graphene scrolls; nitrogen doping; MnO nanowires; lithium-ion batteries

There is an urgent demand for searching advanced electrode materials to fulfill the ever-growing needs in building next-generation Li-ion batteries (LIBs). Transition metal oxides (TMO_x, where TM is Co, Mn, Sn, Fe etc.) have been touted as promising anode candidates owing to their high specific capacities exceeding that of traditional graphite material (372 mAh g^{-1}).[1-4] For example, MnO and MnO_2 can deliver capacity values beyond 750 mAh g^{-1} through conversion reactions.[5] In view of multiple electron-transfer per metal center, on the other hand, conversion reactions inevitably bring a series of thermodynamic and kinetic problems for TMO_x electrodes, such as limited capacity release, poor cycle life, and huge volume change. Nanostructure engineering together with carbon hybridization have paved an avenue for tackling these issues. Particularly, nanostructuring TMO_x to diverse geometric shapes including zero-dimensional (0D) nanoparticles (NPs),[6,7] 1D nanowires/nanorods,[8,9,10] and 2D nanosheets[11,12] enable more active sites and shorter Li^+ diffusion paths. In addition, hybridizing these nanostructured TMO_x with conductive carbon allows fast electron transport and buffers volume variation. These strategies have been proposed for the synthesis of TMO_x/C core-shell nanorods, graphene-loaded NPs, coaxial TMO_x/C nanowires etc.[6-12] Despite their potentials, the integrity maintenance of these materials during cycling is still a challenge, because the introduced carbon matrices with limited elasticity are vulnerable to

cracking as a result of the expanded TMO_x core, rendering the hybrid framework ineffective in upholding electrode integrity for long-life LIBs.

Graphene scroll (GSC), an emerging important member of graphitic carbon family, is normally shaped by scrolling 2D graphene sheets (GS) with a 1D tubular structure resembling that of multi-walled CNTs.[13,14] Owing to the characteristic open topology, GSC enables wrapping foreign nanomaterials into its interior cavities, and besides, the elastic tubular walls of GSC can facilitate the radial expansion to accommodate the increasing volume during the ion intercalation process.[15-18] This feature could inspire a new strategy to address some drawbacks existing in TMO_x anodes, such as large volume change and poor cycle stability. However, due to the technique difficulties in preparing GSC, only few efforts have been made so far on successful fabrication of GSC-based TMO_x hybrid electrodes for LIBs. Yan et al. reported a cold quenching method for wrapping Fe_3O_4 NPs with GSC, which show enhanced cycle stability.[17] Mai and co-wrokers used V_3O_7 nanowires as template to prepare GSC-wrapped V_3O_7 nanowires, and it can retain 87.3% capacity retention after 400 cycles.[18] Indeed, these 1D hybrids substantially mitigate the volume expansion of the oxides benefited from the geometry confinement of GSC shell. Nevertheless, a truly durable high rate capability for these 1D hybrids has not been realized because the electron transfer that is strictly constrained at least in one dimension is still discontinuous in these electrodes. Therefore, the ambipolar (ionic and electronic) diffusion is relatively sluggish, which slows down the transport kinetics in the entire batteries, and leads to the limited rate capabilities.

One efficient way to resolve the above-discussed problem is to build a electrode that consists of robust 3D cross-linked architecture assembled both by continuous interconnected 1D and 2D nanoscaled building blocks.[19,20] Such a hierachical 3D structure can provide not only direct and rapid electron/ion transport paths in the radial direction, but also long-range conductive channels along the axial direction.[21,22] Hence, the kinetics problems caused by material structure-induced diffusion limitation can be minimized so as to enhance the

electrode reaction. Nevertheless, to our knowledge, there is no report to date regarding the design of 3D hierachical GSC/TMO_x-based architecture with integrated multi-dimensional building blocks, and thus fabricating such kind of hybrid electrodes through a facile and viable synthesis approach still remains a great challenge.

Here, we highlight a strategy to engineer a 3D hierachical GSC/TMO_x-based anode configuration composed of ultralong 1D porous MnO nanowires (NWs) sheathed in nitrogen-doped graphene scrolls (N-GSC) which themselves embedded in continuous cross-linked networks of 2D N-doped graphene ribbons (GN) (denoted as MnO@N-GSC/GR). Building such a 3D hierachical structure relies on the formation of nanowire templated N-dopped GSC architecture through the self-scroll of GS in a hydrothermal-assisted self-assembly and N-doping process. Ultralong 1D MnO_2 NWs are used both as precursor and template to induce the oriented scrolling of GS along the nanowire surface, followed by an in-situ transformation of MnO_2 into MnO through carbon thermal reduction by annealing treatment. Such a phase transition process leads to the formation of porous MnO NWs with plenty of internal voids, whilst each of the porous nanowires is uniformly entrapped into the interior cavity of GSC to form a unique core-sheath coaxial nanocable. In virtue of the structural and interfacial engineering that assembly of sheathed 1D nanowire with 2D GN into an ordered 3D hierarchical network, it is anticipated that such a unique MnO/graphene heterostructure would simultaneously addresses the key issues required for LIBs: (i) the multi-scaled and multi-dimensional integration affords 3D continuous conductive networks and interconnected open diffusion channels for rapid electron and ion transport, promoting the reaction kinetics of the whole electrode. (ii) enwrapping MnO NWs with robust GSC prevents the NWs from aggregating, and also enables the formation of solid electrolyte interphase (SEI) around GSC surface instead of on MnO/electrolyte interface, keeping the SEI layer from cracking during repetitive volume expansion and contraction. (iii) the internal stress induced by large volume change of MnO upon Li^+ insertion/extraction can be buffered through the accommodation of

elastic GSC walls along with available voids inside the core-sheath structure, ensuring the structural integrity of electrode. (iV) doping nitrogen heteroatoms into the graphene-backboned networks can significantly boost the electrical conductivity and surface wettability of electrode, facilitating fast charge transfer at the electrode/electrolyte interface.[23,24] As a consequence, the as-built 3D MnO@N-GSC/GR electrode shows outstanding lithium storage performances in terms of reversibility, ultrahigh rate capability (349 mAh g^{-1} at 8.0 A g^{-1}; 205 mAh g^{-1} at 15.0 A g^{-1}), and long-life span (812 mAh g^{-1} remained after 1000 cycles at 2.0 A g^{-1}), hence holding great potential as advanced anodes for high-efficiency LIBs.

Scheme 1 illustrates the synthesis process of the MnO@N-GSC/GR. Ultralong single-crystalline MnO_2 NWs (aspect ratio > 1000) are first prepared by a hydrothermal method (**Figure S1**a-d, Supporting Information). The surfaces of these MnO_2 NWs are then positively charged by physical adsorption of cationic polyelectrolyte, poly(diallydimethylammonium chloride) (PDDA), in order to drive a close combination with negatively charged graphene oxide (GO) through electrostatic attraction. The surface charges are evidenced by zeta potential (+15~+47 mV for the PDDA-modified MnO_2 NWs and -26~-42 mV for the GO, **Figure S2**a). In this case, the co-assembly process affords a tight and uniform connection between MnO_2 NWs and GO sheets, thereby organizing into a continuous ribbon-like framework (Figure S2b). The obtained GO-adhered MnO_2 NWs (MnO_2/GO) are then dispersed in a urea-dissolved aqueous GO suspension and placed in an autoclave for hydrothermal treatment. During this process, GO is hydrothermally reduced to graphene accompanying with N-doped by urea, while the planar graphene sheets adhered on the MnO_2 NWs directionally roll up into tubular graphene scrolls along the nanowire surface, which synchronously enwrap MnO_2 NWs within the scrolls to form 1D core-sheath coaxial nanocables (MnO_2@N-GSC). Benefiting from residual oxygen-containing groups serving as cross-linking sites, the exposed graphene surface of MnO_2@N-GSC is interlinked with additional graphene sheets, both of which act as building blocks to further self-assemble into a

3D macroscopic hydrogel under the driving force of enhanced π–π stacking and hydrophobic interactions as a result of the decreased oxygenated groups on graphene.[25] After freeze-drying dehydration and annealing treatment in Ar atmosphere, the final 3D hierarchical foam-like MnO@N-GSC/GR is obtained by simultaneously thermal-induced carbon reduction of MnO_2 and deep deoxidization of graphene (the photograph illustration of the synthetic procedure is shown in **Figure S3**).

The wrapping of MnO_2 NWs by GS into 1D core-sheath MnO_2@N-GSC nanocables is the critical step to achieve such a desired 3D hierarchical architecture. To gain further insights into the evolution process of the MnO_2@N-GSC, samples obtained from different stages of hydrothermal treatment are characterized. Field-emission scanning electron microscopy (FESEM) analysis reveals that the core-sheath MnO_2@N-GSC nanocables evolve from the nanowire-induced self-scrolling of GS, as depicted in **Figure 1**a(1-4) and 1b. At the early stage of hydrothermal treatment, MnO_2 NWs are closely overlaid by continuous cross-linked GO ribbons (Figure 1a1). As the reaction proceeds, GO is reduced gradually, and the attractive interaction between the reduced GO and MnO_2 NWs drives some graphene sheets to bend along the nanowire in the radial direction (Figure 1a2),[18] resulting in some gaps emerged between the cross-linked GO sheets. Later, the bended graphene sheets tend to further scroll directionally surrounding the nanowire surface, accompanied with more voids coming out and an increase in the thickness of nanowire (Figure 1a3). Eventually after reaction for 3 h, the original smooth MnO_2 NWs evolve into well-defined core-sheath coaxial nanocables composed of MnO_2 nanowire core and GSC sheath (Figure 1a4). It is worth mentioning that in addition to assist in forming nanowire templated GSC architecture, the hydrothermal process has no effect on the phase transition of MnO_2, as verified by the X-ray diffraction (XRD) characteristic peaks of α-MnO_2 before and after hydrothermal treatment, as shown in **Figure S4**.

The morphology and microstructure of the as-formed MnO@N-GSC/GR are examined using FESEM and transmission electron microscopy (TEM). Typical FESEM images at different magnifications, as shown in **Figure S5** and Figure 1c-f, reveal the multi-dimensional ordered hierarchical architectures of MnO@N-GSC/GR. At low magnification (Figure 1c and 1d; Figure S5a and b), one can see that numerous wire-shaped MnO@N-GSC are embedded in 3D nested GR networks consisting of interwoven GS. The higher magnification FESEM images exhibit that very thin GSC layer appears at the edge of resultant MnO NWs (Figure 1f), around where large-area graphene ribbons serve as a binder to connect the separated nanowires together (Figure 1e). Clearly, the wheatear-like MnO NWs, with an ultralong length over tens of micrometers and a diameter range of 100–200 nm, inherit the 1D shape from the MnO_2 NWs precursor, but their skeletons become somewhat rough and loose, owing to the structural shrinkage caused by the phase conversion of MnO_2 to MnO during the annealing process.[26] Aligned crystal domains form while leaving nanosized voids inside the core-sheath MnO@N-GSC nanocables (Figure 1f). Notably, the morphology of the MnO@N-GSC/GR is different from that of the sample obtained by direct annealing MnO_2 NWs, which mechanically mixed with GO (denoted as MnO/G) without hydrothermal treatment (**Figure S6**). In MnO/G, an obvious agglomeration of the MnO NWs emerges after the annealing treatment, and there is no graphene wrapping layer visible around the nanowire surface, but only thick and dense graphene flakes randomly attached to the stacked nanowire bundles. Detailed information on the hierarchical structure of MnO@N-GSC/GR is further elucidated by TEM and high-resolution TEM (HRTEM) observation. A magnified TEM image (Figure 1g) clearly shows that the porous MnO NWs have been fully and uniformly wrapped by GSC so as to form an internal-void-rich core-sheath nanostructure. From the well-resolved lattice fringes of one nanowire (Figure 1h), the interplanar spacing from the internal core (inset in Figure 1h) is calculated to 0.26 nm, consistent with the distance of the (111) plane of cubic MnO,[27] while the thickness of the external GSC sheaths is determined to be around 4 nm

(~5-8 layers). This further demonstrates that the porous MnO NWs have been scrolled into the interior cavities of GSC. The cross-sectional energy dispersive spectroscopic (EDS) line scan results (inset in Figure 1i) obtained from the high-angle annular dark-field scanning TEM (HAADF-STEM) image (Figure 1i) also confirm the well-defined core-sheath nanocables with MnO core and N-doped graphene sheath. The corresponding EDS elemental mapping from the HAADF-STEM image (Figure 1j) further shows a uniform distribution of Mn, C, O, and N elements in MnO@N-GSC/GR, in which Mn and O distribute evenly across the whole nanocables. It is worth mentioning that N distributes over all scope uniformly, suggesting that N heteroatoms are homogeneously doped both in GSC and GR.

X-ray photoelectron spectroscopy (XPS) is used to detect the composition and chemical state of MnO@N-GSC/GR. The survey scan XPS spectrum (**Figure 2**a) shows the presence of Mn 2p, Mn 3s, Mn 3p, O 1s, C 1s, and N 1s with no evidence of impurities. The high resolution XPS spectrum of Mn 2p doublet (Figure 2b) with two peaks located at 641.8 eV for Mn $2p_{3/2}$ and 653.3 eV for Mn $2p_{1/2}$ is characteristic to MnO.[28] Figure 2c and 2d compare the C 1s high resolution XPS spectra of GO and MnO@N-GSC/GR, in which dramatic loss of oxygen-containing functional groups indicates the reduction of GO. The high resolution XPS spectrum of N 1s of MnO@N-GSC/GR (Figure 2e) can be resolved into three components centered at 397.9, 399.6 and 401.8 eV, representing the pyridinic, pyrrolic and graphitic types of N atoms, respectively.[29] In addition, the XPS analysis reveals that the N-doping level was 4.8 at%. The carbon content of MnO@N-GSC/GR is also evaluated by thermogravimetric analysis (TGA) together with elemental analyses (EA). TGA result (**Figure S7**) shows that the weight fraction of carbon in MnO@N-GSC/GR is about 15.6%, which nearly matches with the result from EA (16.0%). XRD analysis is conducted to identify the crystalline phase of MnO@N-GSC/GR. As seen in typical XRD pattern (Figure 2f), the diffraction peaks located at 34.9°, 40.7°, 58.9°, 70.3° and 73.9° can be indexed to a pure face-centered cubic (fcc) MnO (JCPDS no. 07-0230), while a diffraction hump appearing between 24° and 28°

can be attributed to the N-doped graphene backbone.[30] For comparison, the XRD patterns of samples including MnO/G and N-doped graphene foam (denoted as N-GF) are also given in Figure 2f. Except for the weak peak at 26° corresponding to the stacking of graphene sheets, other diffraction peaks are well indexed to pure fcc MnO in MnO/G.

Raman spectroscopy is adopted to evaluate the graphitic quality of MnO@N-GSC/GR, as shown in Figure 2g. There are two typical D and G bands at around 1334 and 1589 cm^{-1} corresponding to the sp^3-type disordered carbon and the sp^2-type ordered graphitic carbon, respectively.[31] Compared with GO (I_D/I_G = 1.02), an increased ratio of D band to G band (I_D/I_G = 1.14) in MnO@N-GSC/GR suggests the reduction of GO with more defects and disordered structure after N-doping.[32] In addition, a notable Mn-O vibrational band appears at 648 cm^{-1}, confirming the presence of MnO in MnO@N-GSC/GR.[33] The electrical conductivity of MnO@N-GSC/GR is further measured to be 50.1 S m^{-1} using a four-point probe method, almost 2 and 3 orders of magnitude greater than that of MnO/G composite (24.7×10^{-2} S m^{-1}) and pristine MnO_2 NWs (39.4×10^{-3} S m^{-1}), indicating that the disordered structure of graphene backbone after N-doping improves the electronic conductivity.[23] Figure 2h shows the Fourier transform infrared spectroscopy (FT-IR) analysis results. In contrast to GO, the characteristic absorption bands of the oxygen-containing groups in GO (peaks at 1054, 1224, 1400, and 1730 cm^{-1}) are vanished after annealing, indicating an extensive decomposition of alkoxy, hydroxyl, epoxy, and carboxyl in MnO@N-GSC/GR.[34,35] Besides, a distinct absorption band attributed to the Mn-O-C bond at 1114 cm^{-1} suggests that there is a strong interaction between MnO and graphene backbone in MnO@N-GSC/GR.[36] N_2 isothermal adsorption/desorption measurement (Figure 2i) is also carried out to further characterize the porous structure of MnO@N-GSC/GR. Owing to the open pores formed by the internal void between sheath and core together with the gap among the stacked GS, MnO@N-GSC/GR has a high Brunauer-Emmett-Teller (BET) surface area of 105.3 m^2 g^{-1} along with a Barrett-Joyner-Halenda (BJH) pore size distribution of 3-110 nm (inset in Figure

2i), much higher than that of MnO/G (21.8 m^2 g^{-1}) and pristine MnO_2 NWs (2.7 m^2 g^{-1}) (**Figure S8**). The high surface area of MnO@N-GSC/GR combined with its unique macro- and meso-porous feature is necessary for efficient electrolyte penetration and fast ion access, and also helpful to cushion the volume expansion of MnO upon cycling.

As a demonstration, the as-prepared 3D hierarchical MnO@N-GSC/GR is evaluated as an anode material for LIBs to highlight the merits of this unique architecture. The cyclic voltammetry (CV) measurements of the MnO@N-GSC/GR electrode, as shown in **Figure 3**a, are performed for the first four cycles. In the first cathodic scan, the sharp peaks observed below 0.5 V corresponds to the initial reduction of MnO to metallic Mn ($MnO + 2Li^+ + 2e^- \rightarrow Mn + Li_2O$) as well as the formation of SEI layer.[2,37] The reduction peak shifts to about 0.45 V since the second cycle, which can be ascribed to improved kinetics and microstructure alterations of electrode after the first lithiation process. Either in the first anodic scan or in subsequent cycles, one broad peak centered around 1.3 V is observed owing to the oxidation of metallic Mn ($Mn + Li_2O \rightarrow MnO + 2Li^+ + 2e^-$) and Li_2O decomposition.[27] Note that there is another weak oxidation peak remained at about 2.07 V with cycling proceeded, which can be assigned to the re-oxidization of Mn^{2+} in MnO/graphene hybrid to higher oxidation state manganese (> 2+).[38] After the second cycle, the CV curves are well overlapped, suggesting the relatively stable charge/diacharge process with high electrochemical reversibility. Figure 3b shows typical discharge-charge voltage profiles for the initial four cycles of MnO@N-GSC/GR at a current density of 0.1 A g^{-1}. The first cycle delivers a very high discharge capacity of 1217 mAh g^{-1} and a charge capacity of 862 mAh g^{-1}, yielding an initial Coulombic efficiency of 70.8%. Afterwards, the Coulombic efficiency goes up to 95.3%, 97.5%, and 98.4% for the second, third, and fourth cycle, respectively. The initial irreversible capacity loss could be mainly attributed to the consumption of Li^+ to form the SEI layer and irreversible insertion of Li^+ into the defects on GSC and GR.[9,27] Notably, the initial discharge-charge profiles deliver well-defined and flat discharge plateaus (lithiation process)

in range of 0.2−0.55 V as well as the corresponding sloped charge plateaus (delithiation process) between 1.2 and 1.5 V.

The rate capabilities of electrodes are further explored. The assembled cell using MnO@N-GSC/GR as active materials is first tested at the same charge and discharge current densities of 0.1 A g^{-1}, and then at increased current densities from 0.2 to 8.0 A g^{-1}. As seen in Figure 3c, the average reversible capacity of MnO@N-GSC/GR at a current density of 0.1 A g^{-1} is 855 mAh g^{-1}, much higher than that of MnO/G (629 mAh g^{-1}) and MnO_2 NWs (381 mAh g^{-1}). Even at the relatively high current density of 1.0, 2.0, 4.0, and 8.0 A/g, MnO@N-GSC/GR still exhibits the high average discharge capacity of 765, 657, 506, and 349 mAh g^{-1}, respectively. It is worth pointing out that in view of the relatively low carbon content in MnO@N-GSC/GR (15.6%), there should be a very limited capacity contribution from the N-doped graphene backbone, which is also validated by the rate and cycle tests for N-GF (**Figure S9**). After the high-rate charge/discharge at 8.0 A g^{-1}, the average capacity of MnO@N-GSC/GR electrode gradually increase to 1060 mAh g^{-1} when scanned again at 0.1 A g^{-1}, highlighting the excellent Li^+ storage reversibility. On the contrary, MnO/G and MnO_2 NWs not only deliver negligible discharge capacities of ca. 37 and 6 mAh g^{-1} at the high current rate of 8.0 A g^{-1}, respectively, but also hardly recover the capacity even when the current rate is switched back to 0.1 A g^{-1}. Obviously, the capacity difference at high rate between these materials should originate from the specific electrode configuration. In MnO/G electrode, the disconnected networks lead to sluggish ion transport and especially inferior electrical conductivity at high current rates exceeding 0.5 A g^{-1}, making part of MnO active materials inaccessible to Li^+ and then ineffective enough to adapt extremely fast electron transfer. In contrast, the 3D hierachical porous MnO@N-GSC/GR electrode architecture with interconnected networks of N-doped 1D GSC and 2D GR offers fast electron and Li^+ transport channels both in axial and radial directions along with lower electron conduction barriers as well as shorter ion diffusion lengths. In order to better evaluate the electrochemical

properties in nature, we also make and test a bare MnO@N-GSC/GR electrode without the addition of carbon black (**Figure S10**). Although there is a decline as expected in the rate capability of the bare MnO@N-GSC/GR electrode, it is still competitive to that of MnO/G and MnO_2 NWs (with the addition of carbon black), suggesting intrinsic features of fast and efficient electronic/ionic conductivity of MnO@N-GSC/GR.

To further demonstrate the ability to accommodate ultrafast electron and charge transports toward the 3D hierachical MnO@N-GSC/GR electrode, the rate test is carried out at even higher current densities from 0.5 to 15.0 A g^{-1}. As shown in Figure 3d, the MnO@N-GSC/GR electrode still delivers high average reversible capacities of 801, 727, 635, 492, 338, and 281 mAh g^{-1}, when cycled at the current densities of 0.5, 1.0 , 2.0, 4.0 , 8.0 , and 10.0 A g^{-1}, respectively. Particularly, the average discharge capacity of 205 mA h g^{-1} can be achieved even at the ultrahigh current rate of 15.0 A g^{-1} (charge/discharge time: ~40 s), which is the highest rate capability so far for MnO-based anode materials (**Figure S11**). Moreover, the MnO@N-GSC/GR electrode can quickly respond to the drastic change of current density, since the discharge capacity can still be recovered to be ~862 mAh g^{-1} when the current density is switched from 15.0 to 0.5 A g^{-1}.

The discharge rate performance of MnO@N-GSC/GR is subsequently surveyed with the cells charged at a constant current density of 0.1 A g^{-1} and then discharged at the current densities varying from 0.1 to 8.0 A g^{-1} (Figure 3e). The MnO@N-GSC/GR electrode is able to deliver stable reversible capacities of ca. 651, 585, and 502 mAh g^{-1} at the discharge current densities of 2.0, 4.0, and 8.0 A g^{-1}, respectively, indicating the fast and efficient capacity release of MnO@N-GSC/GR at high discharge current rates. Meanwhile, the charge rate performance of cells is also investigated by fixing the discharge current rate to 0.2 A g^{-1} and then increasing the charge current rates from 0.2 to 8.0 A g^{-1} (Figure 3f). The MnO@N-GSC/GR electrode exhibits a charge capacity of 822 mAh g^{-1} after 0.2 A g^{-1} charging, while the capacity can still retain 713 and 657 mAh g^{-1} at 4.0 and 8.0 A g^{-1} charging, representing

that about 86.7% and 79.9% of the initial capacity can be rapidly charged in the charge time of ~10 and ~5 min using the constant current mode of 0.2 A g^{-1}, respectively. Such impressive discharge and charge rate performances are of great significance to the development of high current transmission (high power) devices for electric vehicle applications.

In addition to ultrahigh rate capability, the unique 3D hierarchical architecture also endows the MnO@N-GSC/GR with excellent cyclic stability. The discharge capacity vs. cycle number and corresponding Coulombic efficiency of the MnO@N-GSC/GR electrode at a constant discharge/charge rate of 0.2 A g^{-1} is depicted in **Figure 4**a, in which the cycling performances of MnO_2 NWs and MnO/G electrodes are shown as well for comparison. The initial reversible capacity of MnO@N-GSC/GR electrode is around 805 mAh g^{-1}, which gradually reaches to the capacity value as high as 1202 mAh g^{-1} after 100 continuous cycles. This reversible capacity at the end of 100 cycles is much higher than that of MnO/G (462 mAh g^{-1}) and MnO_2 NWs (226 mAh g^{-1}) electrodes under the same testing condition. Also, a nearly 100% of Coulombic efficiency is achieved throughout the overall cycling operation. Notably, the specific capacity of MnO@N-GSC/GR after cycles is much higher than the theoretical capacities both of MnO (756 mAh g^{-1}) and graphite (372 mAh g^{-1}), which has been widely reported for most transition metal oxides-based anode materials. Such a activation process is probably caused by the growth of an electrochemically gel-like polymer layer,[27] as well as the larger electrochemical active surface area of the porous architecture, which can enhance Li^+ storage.[9,39] Another reason can be related to the generation of higher oxidation state manganese (Mn^{4+}) during charge/discharge process as verified by aforementioned CV analysis.[2,38] This can be also reflected in the discharge-charge voltage curves at different cycle times. As shown in **Figure S12**, a short charge slope at around 2.10 V appears, gradually broadens, and finally transforms into a long plateau upon cycling, indicating an ever-increasing capacity and Li^+ reactivity. In the 50th and 100th discharge/charge curves, there is a discharge plateau at around 0.43 V and two charge plateaus at about 1.34 and 2.10 V,

consistent with those of manganese oxides (Mn^{4+}).[27] This is proved by the subsequent XPS measurements on the valence states of Mn ions in the MnO@N-GSC/GR electrode after 100 cycles (**Figure S13**). Long-term cycle stability of the MnO@N-GSC/GR is further investigated at a high rate of 2.0 A g^{-1}. As shown in Figure 4b, the specific capacity also increases gradually as high as ~1195 mAh g^{-1} until around 400 cycles, before easing back and keeping stable for the subsequent cycles. With prolonged 1000 cycles, the MnO@N-GSC/GR electrode can still deliver a stable reversible capacity as high as ~812 mAh g^{-1}. Compared with previously reported MnO/carbonous hybrid anode materials, the 3D hierarchical MnO@N-GSC/GR shows a remarkably enhanced reversible capacity even after long-term, fast, and deep discharge/charge cycling, as summarized in Table S1.

To disclose the correlation between the cyclic stability and structural feature of the electrode materials, we carry out cycle-dependent TEM characterization of the MnO@N-GSC/GR electrodes after the 1000th charging (delithiated state) (inset in Figure 4b, **Figure S14**a-b and **Figure S15**a) and discharging (lithiated state) (Figure S15b). As demonstrated from the TEM images, the overall 1D core-sheath structure of the MnO@N-GSC nanocables is still maintained without obvious pulverization or size variation. And also, owing to the buffer of GSC sheath, it can be seen that the MnO@N-GSC nanocables expand mainly in the axial direction rather than in the radial direction during Li^+ insertion (Figure S15a and 15b). Most importantly, such specific core-sheath heterostructure is indeed efficient to enhance the stability of SEI. As illustrated in Figure 4e, the highly elastic GSC sheath together with enough internal voids around MnO nanowire allows it to expand without disturbing or breaking the outer GSC shell upon cycling, so that the SEI layer formed outside the nanocables is not ruptured and keeps uniform and thin. In contrast, both the MnO/G (Figure 4c and Figure S14c) and MnO_2 NWs (Figure 4d and Figure S14d) electrodes suffer serious structural distortion and fracture only after 100 cycles, mainly due to partial Mn dissolution as well as internal strain caused by drastic volume expansion, which consequently makes the SEI

layers at the surface of exposed MnO and MnO_2 NWs to repeatedly crack and form over continuous cycles leading to thick and incomplete SEI layers (Figure 4e). These results indicate that the as-built MnO@N-GSC/GR architecture is very effective in maintaining the structural and electrical integrity of electrode, which is recognized to be one of the most important factors in ensuring long-life LIBs over continuous discharge/charge cycles.

The exceptional rate capability and outstanding cycle stability of MnO@N-GSC/GR electrodes benefit from the multi-scaled and multi-dimensional ordered 3D hierarchical architecture. The porous MnO NWs confined in tubular GSC sheath are mechanically isolated with each other but electronically well-connected and the N-doped GSC provide a bicontinuous transfer channel for rapid electron and ion transport. Besides, the cross-linked 3D open networks assembled by 2D N-doped GR embedding the MnO@N-GSC nanocables not only increase the mechanical robustness, enable highly conductive paths for electron transfer in all directions, but also offer available space to accommodate electrolyte penetration for efficient ion access. As stated, the electrochemical impedance spectra (EIS) of MnO@N-GSC/GR, MnO/G, and MnO_2 NWs electrodes are then further measured, as shown in **Figure S16**. All Nyquist plots show a depressed semicircle in the medium-high frequency region, which is associated with charge-transfer resistance in the electrode. The MnO@N-GSC/GR electrode displays a low resistance of about 90.3 Ω (Figure S16a) even after 1000 cycles at high rate, which is significantly lower than that of the MnO/G (267.7 Ω) and MnO_2 NWs (413.4 Ω) electrodes after 100 cycles (Figure S16b). Such a resistance difference is owing to the existence of highly conductive N-doped 3D graphene networks, greatly enhancing the Li^+-reaction kinectics. In addition, the EIS spectra of the MnO@N-GSC/GR electrode before and after 1000 cycles were then compared as well (Figure S16a). Obviously, there is only a slight increase in the charge transfer resistance before (69.1 Ω) and after (90.3 Ω) cycling, further demonstrating the excellent structural integrity.

In summary, we successfully designed and constructed a novel 3D hierarchical MnO@N-GSC/GR anode architecture through nanowire-directed self-scroll of GS in combination with hydrothermal-assisted self-assembly and N-doping strategy. This unique hierarchical heterostructure not only realizes the integration of the advantages of muti-scaled and multi-dimensional building blocks with enhanced electron/ion transfer kinetics, but also succeeds in addressing the structural and interfacial stability issues facing MnO-based anodes. Both advantages ensure the as-built anodes to manifest excellent electrochemical Li-storage properties. Importantly, this facile synthesis strategy can lead to more convenient and competitive routes for fabricating other 1D TMO_x-based advanced electrode materials that experience inferior electron/ion conductivity and SEI instability caused by large volume change (e.g. V_2O_5 NWs, **Figure S17**), and thus it is of great potential for other functional energy storage applications.

Acknowledgements

This work is financially supported by the National Basic Research Program of China (973 program 2013CB934700), the National Natural Science Foundation of China (51502180), Foundation for the Author of National Excellent Doctor Dissertation of China (FANEDD201435), and the Sichuan Province Science and Technology Support Program (2014GZ0093).

[1] M. V. Reddy , G. V. S. Rao, B. V. R. Chowdari, *Chem. Rev.* **2013**, *113*, 5364.

[2] H. L. Wang, L. F. Cui, Y. Yang, H. Sanchez Casalongue, J. T. Robinson, Y. Y. Liang, Y. Cui, H. J. Dai, *J. Am. Chem. Soc*. **2010**, *132*, 13978.

[3] Y. S. Lin, J. G. Duh, M. H. Hung, *J. Phys. Chem. C* **2010**, *114*, 13136.

[4] E. Kang, Y. S. Jung, A. S. Cavanagh, G. H. Kim, S. M. George, A. C. Dillon, J. K. Kim, J. Lee, *Adv. Funct. Mater*. **2011**, *21*, 2430.

[5] L. Ji, Z. Lin, M. Alcoutlabi, X. Zhang, *Energy Environ. Sci.* **2011**, *4*, 2682.

[6] W. J. Yu. L. L. Zhang, P. X. Hou, F. Li, C. Liu, H. M. Chen, *Adv. Energy Mater*. **2015**, *3*, 155.

[7] G. X. Zhao, X. B. Huang, X. K. Wang, P. Connor, J. X. Li, S. W. Zhang, J. T. S. Irvine, *J. Mater. Chem. A* **2015**, *3*, 297.

[8] P. Meduri, E. Clark, J. H. Kim, E. Dayalan, G. U. Sumanasekera, M. K. Sunkara, *Nano Lett*. **2012**, *12*, 1784.

[9] Z. Y. Cai, L. Xu, M. Yan, C. Han, L. He, K. M. Hercule, C. Niu, Z. Yuan, W. Xu, L. Qu, K. Zhao. L.Q. Mai, *Nano Lett.* **2015**, *15*, 738.

[10] H. Jiang, Y. J. Hu, S. J. Guo, C. Y. Yan, P. S. Lee, C. Z. Li, *ACS Nano* **2014**, *8* , 6038.

[11] J. W. Deng, L. F. Chen, Y. Y. Sun, M. H. Ma, L. Fu, *Carbon* **2015**, *92*, 177.

[12] B. Wang, X. Y. Lu, Y. Y. Tang, W. W. Ben, *ChemElectroChem* **2016**, *1* , 55.

[13] L. Viculis, J. Mack, R. Kaner, *Science* **2003**, *299*, 1361.

[14] Z. P. Xu, M. J. Buehler, *ACS Nano* **2010**, *4*, 3869.

[15] Z. Xu, B. N. Zheng, J. W. Chen, C. Gao, *Chem. Mater.* **2014**, *26*, 6811.

[16] X. Xie, L. Ju, X. Feng, Y. Sun, R. Zhou, K. Liu, S. Fan, Q. Li, K. Jiang, *Nano Lett*. **2009**, *9*, 2565.

[17] J. P. Zhao, B. J. Yang, Z. M. Zheng, J. Yang, Z. Yang, P. Zhang, W. C. Ren, X. Y. Yan, *ACS Appl. Mater. Interfaces* **2014**, *6*, 9890.

[18] M. Yan, F. Wang, C. Han, X. Ma, X. Xu, Q. An, L. Xu, C. Niu, Y. Zhao, X. Tian, P. Hu, H. Wu, L. Mai, *J. Am. Chem. Soc*. **2013**, *135*, 18176.

[19] J. W. Long, B. Dunn, D. R. Rolison, H. S. White, *Chem. Rev.* **2004**, *104*, 4463.

[20] H. Jiang, P. S. Lee, C. Z. Li, *Energy Environ. Sci.* **2013**, *6*, 41.

[21] X. L. Wang, W. Q. Han, H. Y. Chen, J. M. Bai, T. A. Tyson, X. Q. Yu, X. J. Wang, X. Q. Yang, *J. Am. Chem. Soc.* **2011**, *133*, 20692.

[22] D. W. Wang, F. Li, M. Liu, G. Q. Lu, H. M. Cheng, *Angew. Chem. Int. Ed.* **2008**, 47, 373.

[23] Z. S. Wu, W. Ren, L. Xu, F. Li, H. M. Cheng, *ACS Nano* **2011**, *5*, 5463.

[24] Y. Chang, J. Li, B. Wang, H. Luo, H. He, Q. Song, L. Zhi, *J. Mater. Chem. A* **2013**, *1*, 14658.

[25] Y. X. Xu, K. X. Sheng, C. Li, G. Q. Shi, *ACS Nano* **2010**, *4*, 4324.

[26] C. B. Zhang, J. G. Wang, D. D. Jin, K. Y. Xie, B. Q. Wei, *Electrochimica Acta* **2015**, *180*, 990.

[27] Y. M. Sun, X. L. Hu, W. Luo, F. F. Xia, Y. H. Huang, *Adv. Funct. Mater*. **2013**, *23*, 2436.

[28] J. F. Moulder , W. F. Stickle , P. E. Sobol , K. D. Bomben , Handbook of X-ray Photoelectron Spectroscopy, (Ed: J. Chastain), Perkin-Elmer Corporation, Eden Prairie, MN **1992**.

[29] H. L. Guo, P. Su, X. Kang, S. K. Ning, *J. Mater. Chem. A* **2013**, *1*, 2248.

[30] W. Wei, S. B. Yang, H. X. Zhou, I. Lieberwirth, X. L. Feng, K. Müllen, *Adv. Mater.* **2013**, *25*, 2909.

[31] K. N. Kudin, B. Ozbas, H. C. Schniepp, R. K. Prudhomme, I. A. Aksay, R. Car, *Nano Lett.* **2008**, *8*, 36.

[32] B. Wang, W. A. Abdulla, D. L. Wang, X. S. Zhao, *Energy Environ. Sci*. **2015**, *8*, 869.

[33] C. Yang, Q. Gao, W. Tian, Y. Tan, T. Zhang, K. Yang and L. Zhu, *J. Mater. Chem. A* **2014**, *2*, 19975.

[34] S. Zhang, L. Zhu, H. Song, X. Chen, B. Wu, J. Zhou, F. Wang, *J. Mater. Chem.* **2012**, *22*, 22150.

[35] M. Acik, G. Lee, C. Mattevi, A. Pirkle, R.M. Wallace, M. Chhowalla, K. Cho, Y. Chabal, *J. Phys. Chem. C* **2011**, *115*, 19761.

[36] S. Zhang, L. X. Zhu, H. H. Song, X. H. Chen, J. S. Zhou, *Nano Energy* **2014**, *10*, 172.

[37] K. J. Zhang, P. X. Han, L. Gu, L. X. Zhang, Z. H. Liu, Q. S. Kong, C. J. Zhang, S. M. Dong, *ACS Appl. Mater. Interfaces* **2012**, *4*, 658.

[38] J. C. Guo, Q. Liu , C. S. Wang , M. R. Zachariah, *Adv. Funct. Mater*. **2012**, *22*, 803.

[39] K. Z. Cao, L. F. Jiao, H. Xu, H. Q. Liu, H. Y. Kang, Y. Zhao, Y. C. Liu, Y. J. Wang, H. T. Yuan, *Adv. Sci*. **2015**, *47*, 4252.

[40]

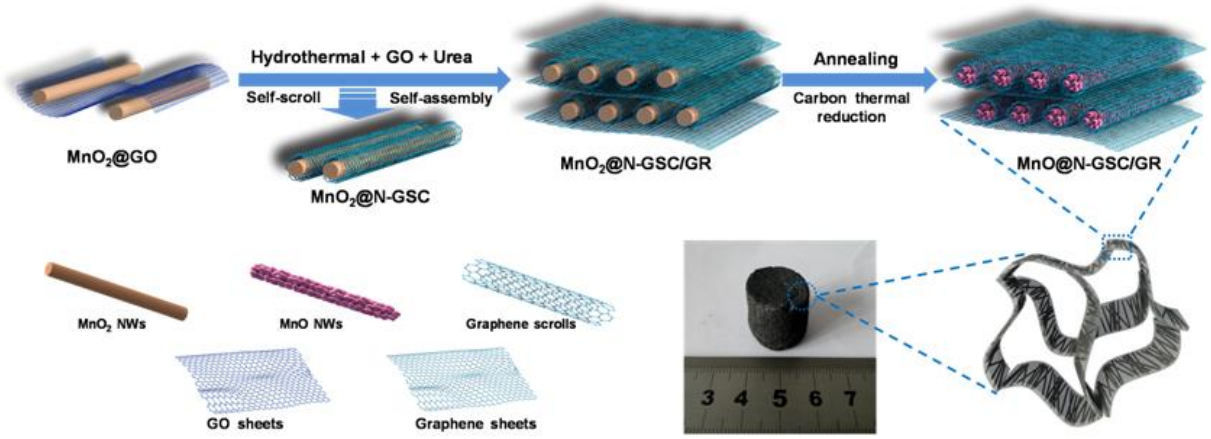

Scheme 1. Schematic illustration of the fabrication process of 3D hierarchical MnO@N-GSC/GR architecture, involving two main steps of the self-scroll and self-assembly process between MnO_2 NWs and GO sheets as well as subsequent annealing treatment.

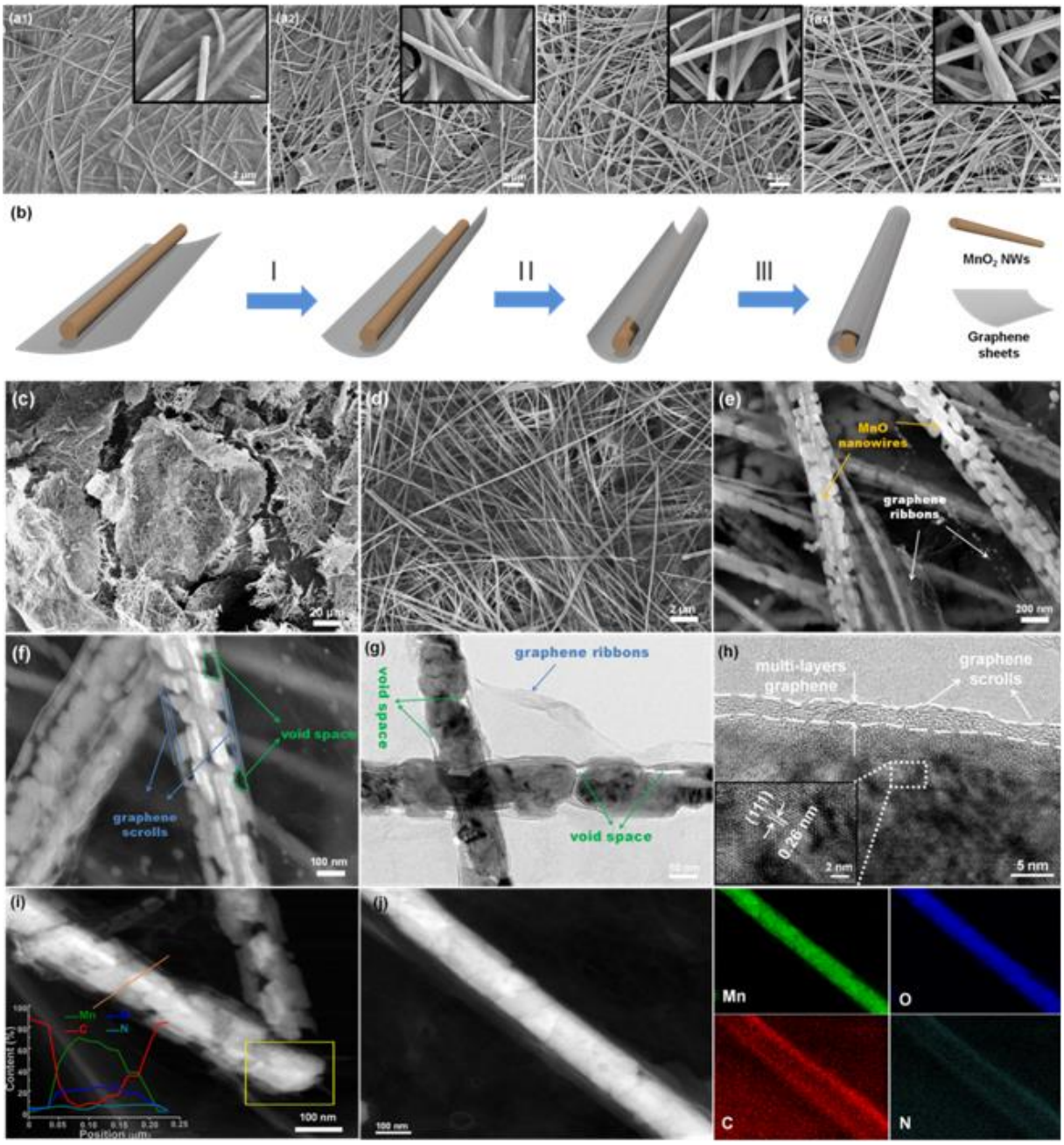

Figure 1 a) FESEM images of samples obtained at different stages of hydrothermal reaction for (a1) 0.5 h, (a2) 1.0 h, (a3) 1.5 h, and (a4) 3.0 h. b) Schematic illustration of the construction process of nanowire templated graphene scrolls. c-f) FESEM images and g,h) TEM images of MnO@N-GSC/GR at different magnifications; the inset of (h) shows the HRTEM image of the nanowire. i,j) HAADF-STEM images with corresponding EDX line scanning profile and elemental mapping images of MnO@N-GSC/GR.

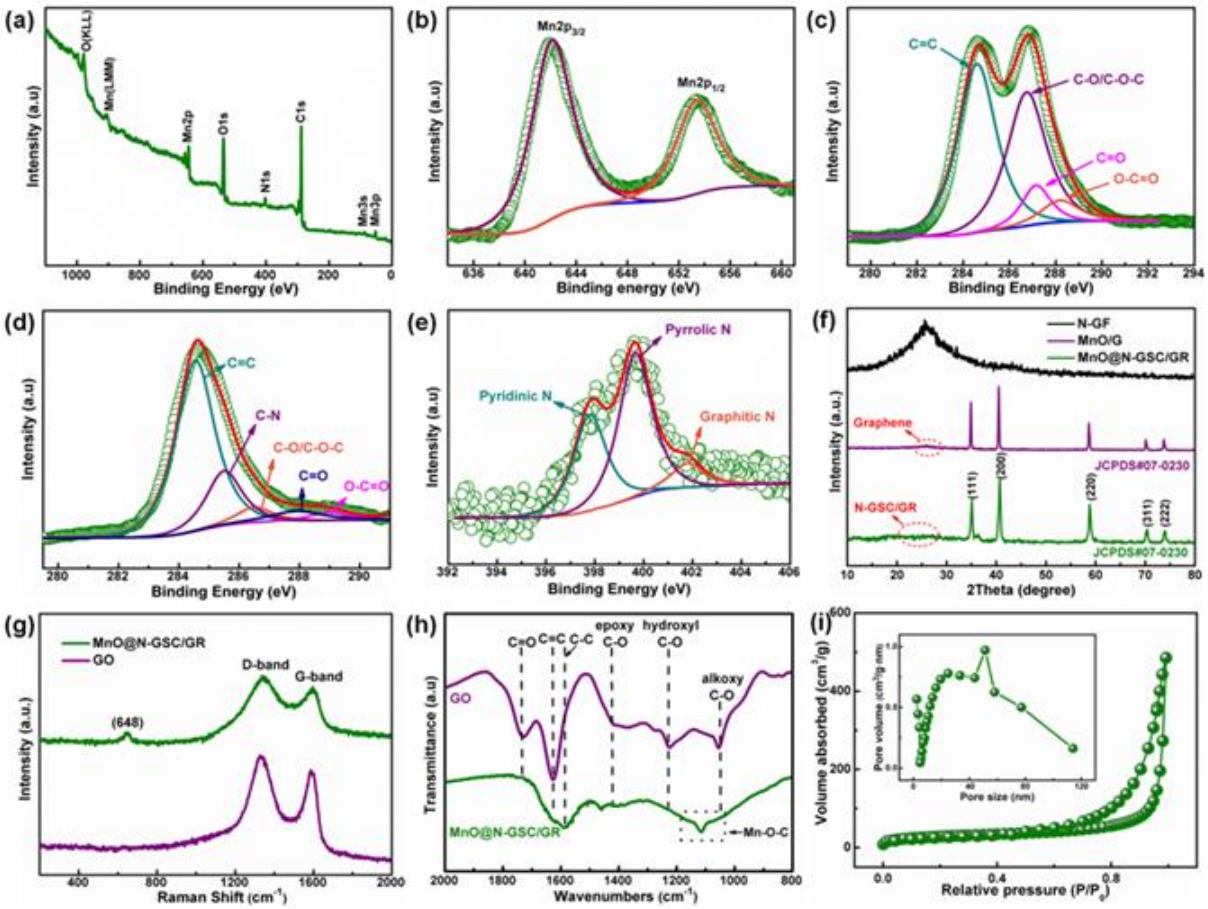

Figure 2 a-d) XPS spectra of MnO@N-GSC/GR and GO: (a) survey scan and high resolution of (b) Mn2p, (d) C1s, and (d) N1s for MnO@N-GSC/GR; (c) high resolution of C1s for GO. f) XRD patterns of MnO@N-GSC/GR, MnO/G and N-GF. g) Raman spectra and h) FTIR spectra of MnO@N-GSC/GR and GO. i) Nitrogen adsorption and desorption isotherm of MnO@N-GSC/GR; the inset of (i) gives the pore-size distribution plot calculated by BJH method from desorption branch isotherm.

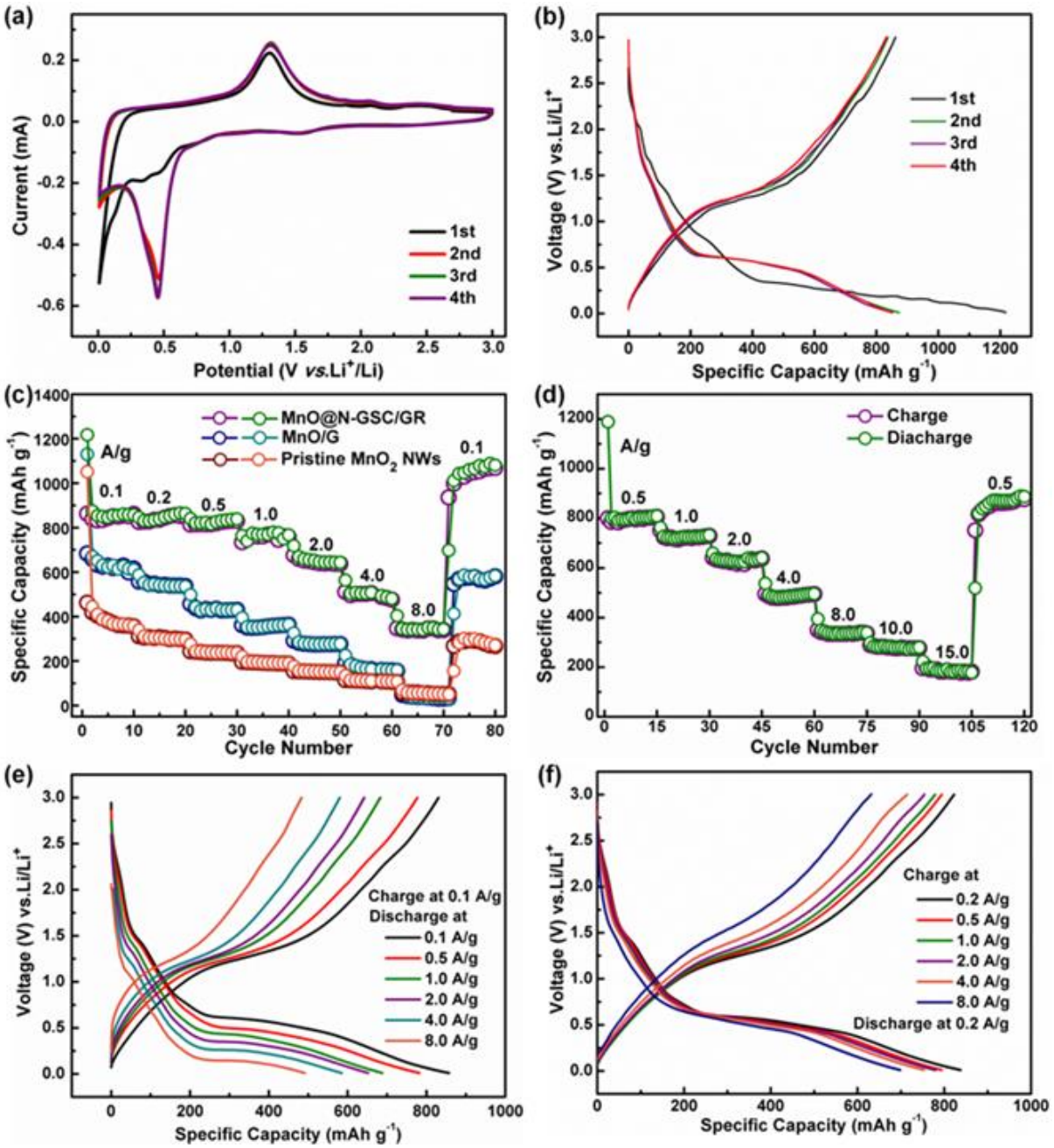

Figure 3 a) Cyclic voltammetry curves and b) discharge-charge voltage profiles of MnO@N-GSC/GR for the initial four cycles. c) Rate capabilities of MnO@N-GSC/GR, MnO/G and MnO_2 electrodes at the current densities of 0.1-8.0 A g^{-1}. d) Rate capability of MnO@N-GSC/GR at the current densities of 0.5-15.0 A g^{-1}. e,f) Discharge-charge voltage profiles of MnO@N-GSC/GR: (e) under the constant charge current density of 0.1 A g^{-1} with discharge rates varying from 0.1 to 8.0 A g^{-1}; (f) under the constant discharge current density of 0.2 A g^{-1} with charge rates varying from 0.2 to 8.0 A g^{-1}.

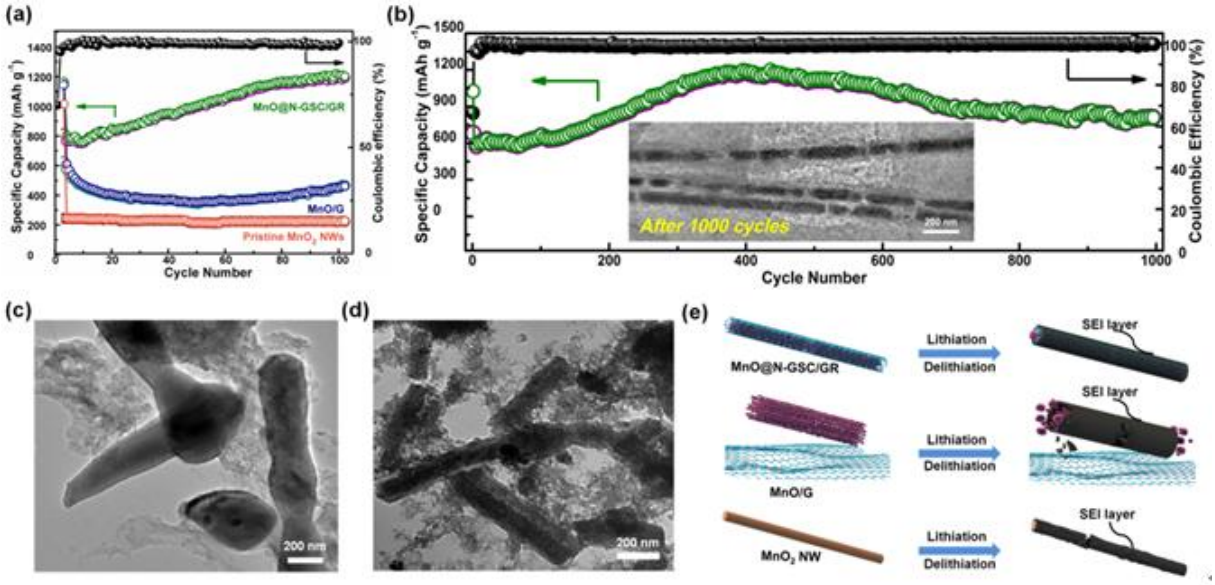

Figure 4. a) Cycling performance of MnO@N-GSC/GR in comparison with MnO/G and MnO_2 NWs at 0.2 A g^{-1} for 100 cycles. b) Prolonged cycling performance of MnO@N-GSC/GR at 2.0 A g^{-1} for 1000 cycles; the inset in (b) shows the TEM image of MnO@N-GSC/GR after 1000 cycles. c,d) TEM images of (c) MnO/G and (d) MnO_2 NWs after 100 cycles. e) Schematic illustration of the advantages of MnO@N-GSC/GR over MnO/G and MnO_2 NWs during lithiation and delithiation process.

Supporting Information

Engineering 3D Hierarchical Anode Configuration Based on Nitrogen-Doped Graphene Scrolled-MnO Coaxial Nanocables for Superior Lithium Storage

Hao Wu, *Penghui Chen*, *Yi Guo*, *Bo Wang*, *Wenjing Liu*, *Heng Liu*, and *Yun Zhang*

1. Experimental Section

Synthesis of MnO_2 NWs precursor: Ultralong MnO_2 NWs were first prepared by a modified hydrothermal method as reported previously.[S16] All chemicals and solvents were purchased from commercial sources and used without purification. In a typical synthesis, 4.0 mmol of $MnSO_4 \cdot H_2O$, 7 mmol of $KClO_3$, 7 mmol of CH_3COOK, and 3.2 mL of CH_3COOH were successively dissolved into 80 mL of distilled water under magnetic stirring to form a homogeneous solution. After that, the solution was sealed in a 100 mL Teflon-lined autoclave, and maintained in an oven at 160 °C for 12 h. The resulting precipitation were collected by centrifugation, washing with distilled water and alcohol for several times, and finally diring in air at 80 ºC.

Preparation of MnO@N-GSC/GR: Typically, the pre-prepared MnO_2 NWs (80 mg) were added into 100 mL of 5 wt% poly(diallydimethylammonium chloride) (PDDA) (Aldrich, M_w=10000-20000, 20 wt%) aqueous solution and ultrasonically treated for 1 h to form uniform dispersion. The excess PDDA was then removed by repeated centrifugation /washing/redispersion cycles. The obtained PDDA-modified MnO_2 NWs aqueous dispersion were further diluted to 100 mL, followed by adding dropwise 20 mL GO (Hengqiu Tech. Inc, Suzhou, China) aqueous suspension (0.75 mg mL^{-1}) under magnetic stirring for 4 h to drive an electrostatic attraction between positively charged PDDA-modified MnO_2 NWs and negatively charged GO sheets. After that, the MnO_2@GO was collected through centrifugation, washing, and then freeze-dried.

MnO@N-GSC/GR was subsequently prepared by a hydrothermal-assisted self-assembly of MnO_2@GO with additional GO sheets in a urea aqueous solution, along with freeze-drying and thermal treatment. In a typical process, dehydrated MnO_2@GO was homogeneously dispersed in 13 mL of urea (70 mg mL^{-1}) aqueous solution, followed by the addition of 2 mL of GO aqueous dispersion (7.5 mg mL^{-1}), and sealed in a 20 ml Teflon-lined autoclave. After hydrothermal treatment at 120 ºC for 3 h, the autoclave was naturally cooled to room temperature, and the formed 3D macroscopic hydrogel was taken out and freezing dried,

followed by annealing at 600 ºC for 2 h in argon steam to generate 3D hierarchical MnO@N-GSC/GR. Also, N-GF was prepared by assembly of GO in a similar hydrothermal process in the absence of MnO_2 NWs.

Prepartion of MnO/G composite: For comparison, MnO/G was prepared through direct annealing MnO_2 NWs simply mixed with GO sheets without hydrothermal treatment. Typically, MnO_2 NWs (80 mg) were first dispersed into 100 mL of distilled water, and ultrasonically treated for 2 h. Then, 20 mL of homogeneous GO (15 mg mL^{-1}) aqueous suspension was added dropwise into the as-dispersed MnO_2 NWs suspension under vigorous magnetic stirring. After stirring for 6 h, the mixed suspension obtained was freeze-dried and then thermally treated by annealing at 600 ºC for 2 h in argon steam to finally obtain MnO/G.

Materials characterization: The phase purity and crystal structure of the products were identified by X-ray diffraction (XRD) using a Bruker DX-1000 diffractometer with Cu-Kα radiation in the 2θ angular range of 10-80 ° at a scanning rate of 0.02 ° s^{-1}. The morphology and microstructure of the products were observed using field emission scanning electron microscopy (FESEM; Hitachi, S4800, 15 kV) coupled with an EDX (Oxford Instrument) spectrometer, and transmission electron microscopy (TEM; JEOL, JEM-2100F) operated at 200 kV equipped with an X-ray energy dispersive spectrometer (EDS). Raman spectra were recorded using a HORIBA Jobin Yvon Raman spectrometer (LabRAM HR) with an Ar^+ laser wavelength of 633 nm at ambient temperature. Fourier transform infrared spectroscopy (FTIR) analyses were performed on a Nicolet 6700 FTIR spectrometer. X-ray photoelectron spectroscopy (XPS) measurements were conducted using X-ray photoelectron spectrometer (Kratos XSAM800). N_2 adsorption/desorption measurements were carried out with Tristar II 3020 instrument at the liquid nitrogen temperature. The specific surface area was calculated using the multipoint Brunauer-Emmett-Teller (BET) method, and the pore size distribution was computed using the Barrett-Joyner-Halenda (BJH) method. Zeta potential measurements were conducted using a Zetasizer 3600 (Malvern Instruments) and both of the modified MnO_2 NWs and GO samples were diluted to 0.35 and 0.1 mg mL^{-1} respectively before measurement. The pH values were adjusted by adding ammonia solution or diluted hydrochloric acid. The elemental analysis was conducted on a Elemental Analyzer (Leeman Labs, Euro EA 3000). Thermogravimetric analysis (TGA) was performed using a Netzsch TG209F1 from room temperature up to 800 ºC at a heating rate of 10 ºC/min under flowing air. The electrical conductivity was measured at room temperature using a ST-2258A digital four-point probe test system (Suzhou Jingge Electronic Co., Ltd). Before measurement, sample powders were

compressed into a wafer with a thickness of 0.2 mm and a diameter of 13 mm by an oil-pressure machine under a pressure of 5 MPa.

Electrochemical measurements: The electrochemical measurements were performed using CR2032 coin-type cells. Working electrodes were prepared by coating homogeneous slurries composed of as-synthesized active materials (80 wt%), acetylene black (10 wt%) and polyvinylidene fluoride binder (10 wt%) dispersed in N-methyl-2-pyrrolidone onto a pure Cu foil. After dried at 80 ℃ for 12h in a vacuum oven, the coated Cu foil was roll-pressed and punched into disks with a diameter of 12 mm. The typical mass loading of active materials was controlled at 1.0-1.2 mg cm^{-2}. The disk as the working electrode was assembled into cells in an Ar-filled glovebox, using lithium metal as the counter/reference electrode, Celgard 2400 membrane as the separate, and 1 M $LiPF_6$ in a mixture of ethylene carbonate (EC), dimethyl carbonate (DMC), and diethyl carbonate (DEC) (volume ratio of 1:1:1) as the electrolyte. The galvanostatic charge and discharge performances were carried out on a multi-channel battery test system (Neware CT-3008W, China) within a potential range of 0.01~3.0 V (vs. Li/Li^+) at different current rates. The electrochemical impedance spectroscopy (EIS) and cyclic voltammetry (CV) tests were conducted by a VMP3 electrochemical workstation (Bio-Logic Inc., Claix, France). The EIS measurements were performed over a frequency range of 100 kHz to 10 mHz with an applied amplitude of 5 mV. The CV experiments were carried out at a scan rate of 0.1 mV s^{-1}.

2. Figures, tables, and related discussion

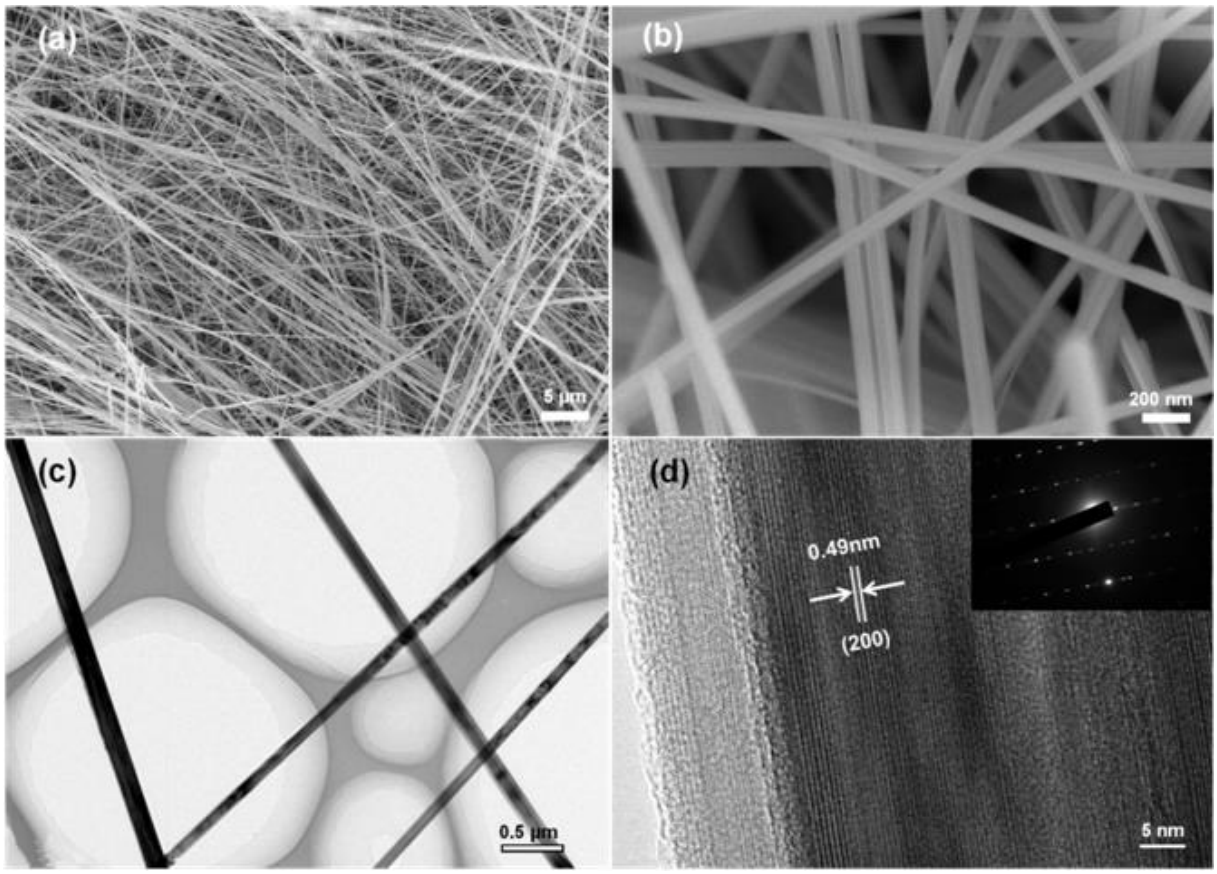

Figure S1. a,b) FESEM images of as-prepared MnO_2 NWs precursor. As shown, the ultralong 1D MnO_2 NWs possess an average diameter of approximately 100 nm and a length of hundreds of micrometers, corresponding to a high aspect ratio of over 1000. c) TEM image and d) HRTEM image of MnO_2 NWs. From (d), the distinct lattice fringes of 0.49 nm in spacing agree well with the interplanar distances of (200) plane of α-MnO_2. In addition, the inset of (d) showing the SAED image also indicates the single crystalline nature of the α-MnO_2 NWs.

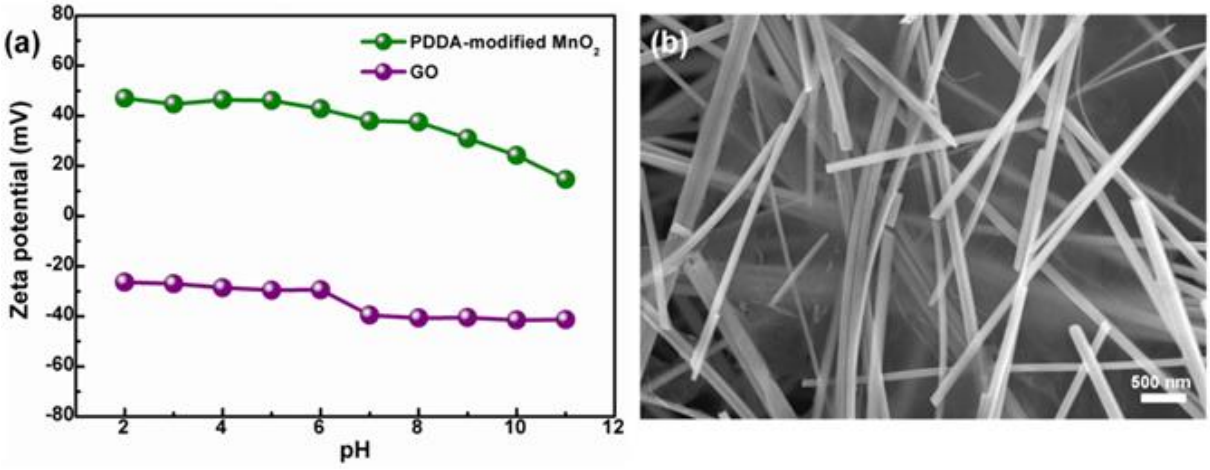

Figure S2. a) Zeta potentials of PDDA-modified MnO_2 NWs and GO in aqueous solutions with various pH values. b) FESEM image of MnO_2 NWs after electrostatic attraction with GO, showing that the mutual assembly can be naturally triggered when modified MnO_2 and GO were oppositely charged, and also revealing that the modified MnO_2 NWs can be anchored by the GO sheets to form a continuous ribbon-like framework.

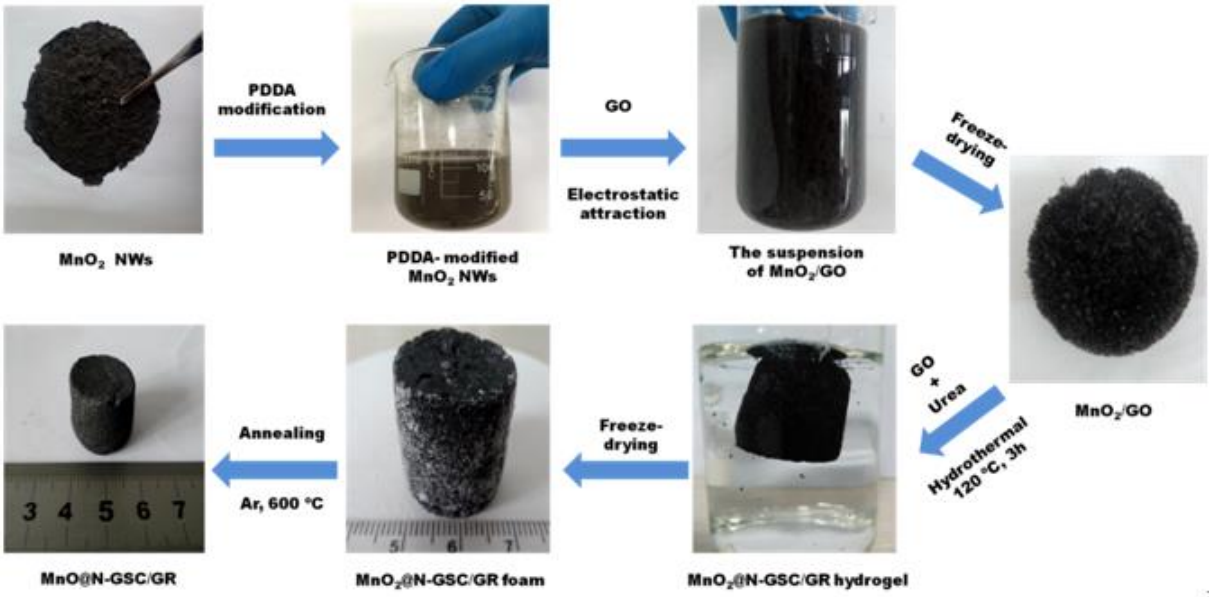

Figure S3. The photograph illustration of the synthetic procedure of MnO@N-GSC/GR.

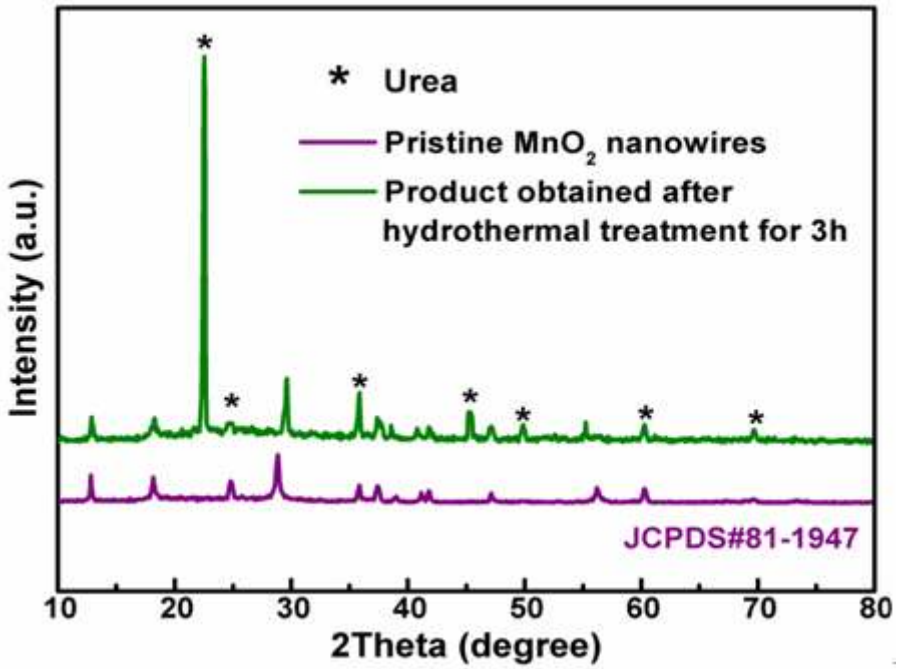

Figure S4. XRD pattern of pristine MnO_2 NWs precursor in comparison with the product obtained after hydrothermal treatment for 3h, suggesting that in addition to the characteristic peaks owing to residual urea, all other XRD peaks of the product after hydrothermal treatment can be indexed to tetragonal α-MnO_2.

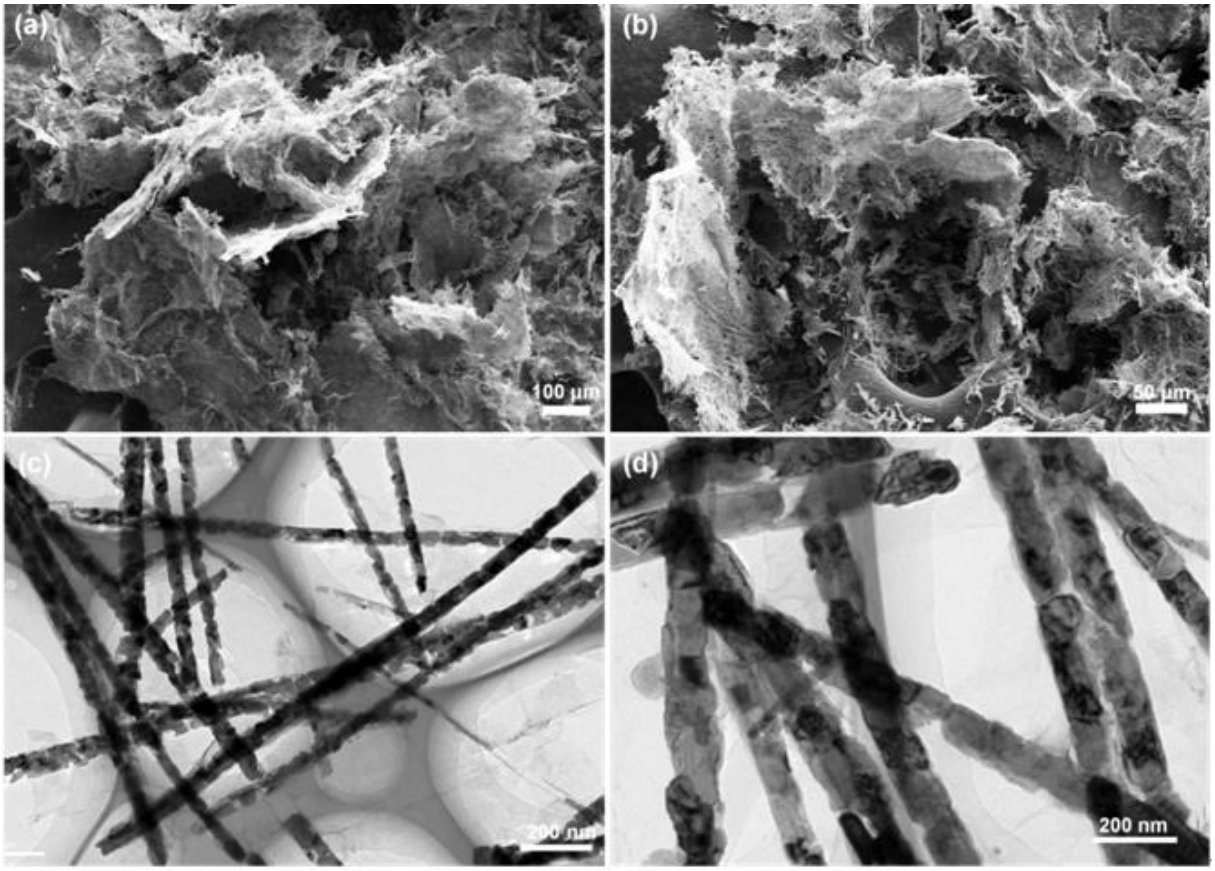

Figure S5. a,b) Low-magnification FESEM images and c,d) TEM images of MnO@N-GSC/GR.

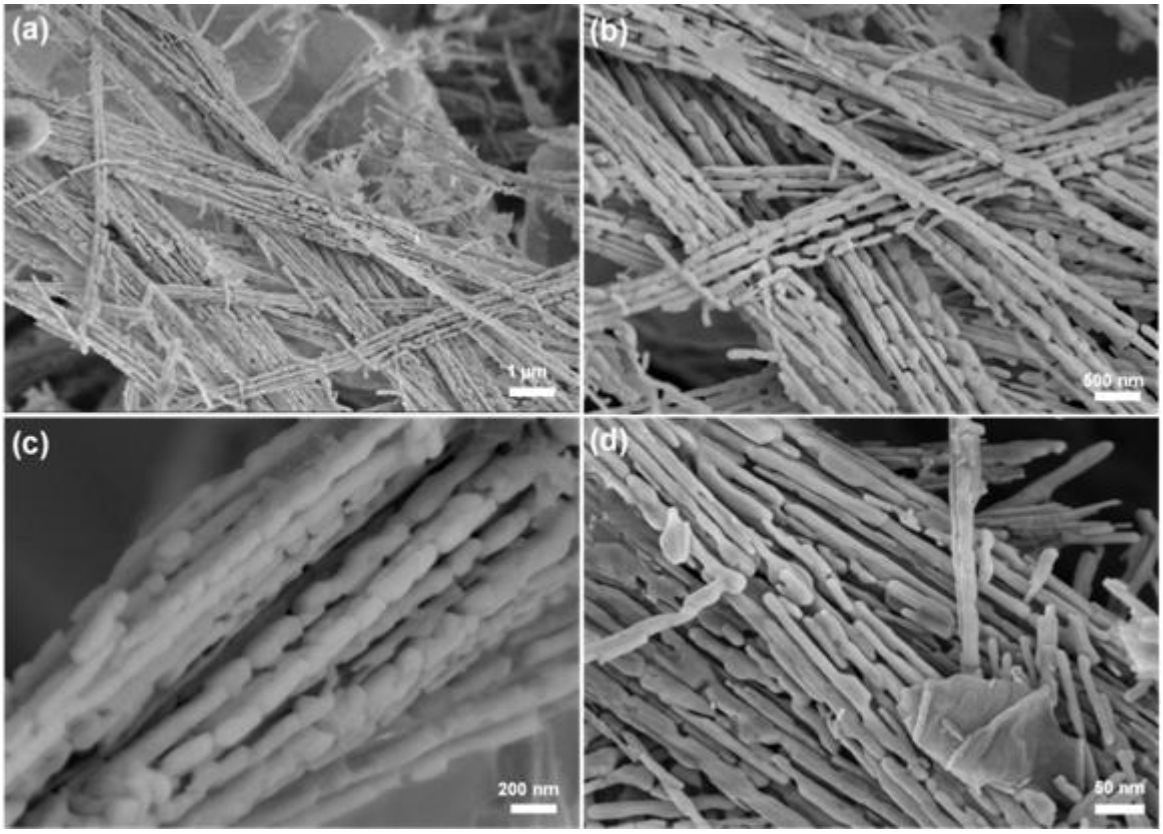

Figure S6. a-d) Typical FESEM images of MnO/G at different magnifications.

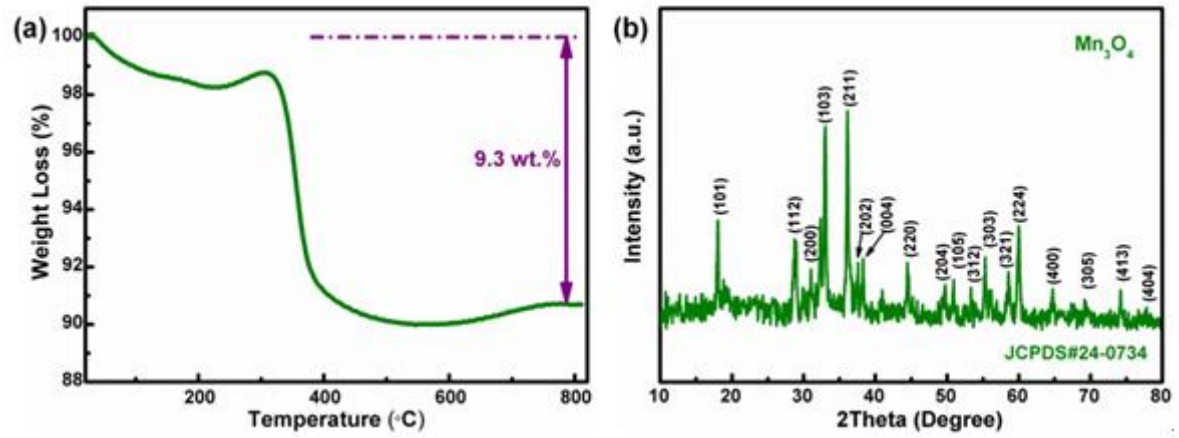

Figure S7. a) TGA curve of MnO@N-GSC/GR. b) XRD pattern of MnO@N-GSC/GR after annealed at 800 ºC in air; it can be seen that the final product after annealing in air belongs to the tetragonal structure of Mn_3O_4 phase (JCPDS# 24-0734), indicating MnO was oxidized to form Mn_3O_4. In theory, this oxidation process will give rise to 7.5 wt.% weight increase. Assumed the total mass is 1 and carbon content is x, then MnO content is (1-x). As shown in the TGA curve, the weight loss can be calculated using the following formula: x-7.5 wt.%(1-x)= 9.3 wt.%. Then the carbon content of x equals to 15.6 wt%.

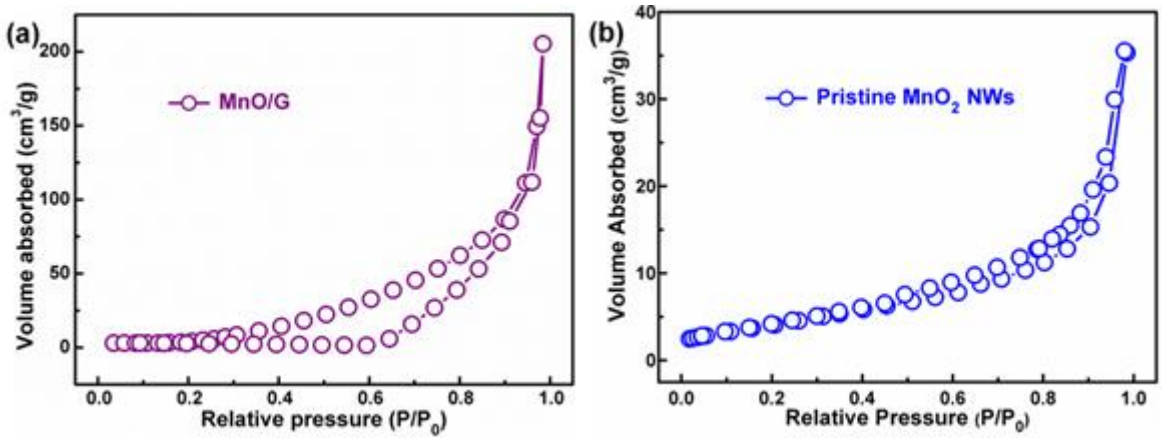

Figure S8. Nitrogen adsorption and desorption isotherm of a) MnO/G and b) pristine MnO_2 NWs. The Brunauer-Emmett-Teller (BET) specific surface area of MnO/G and MnO_2 NWs were measured to be 21.8 and 2.7 m^2 g^{-1}, respectively.

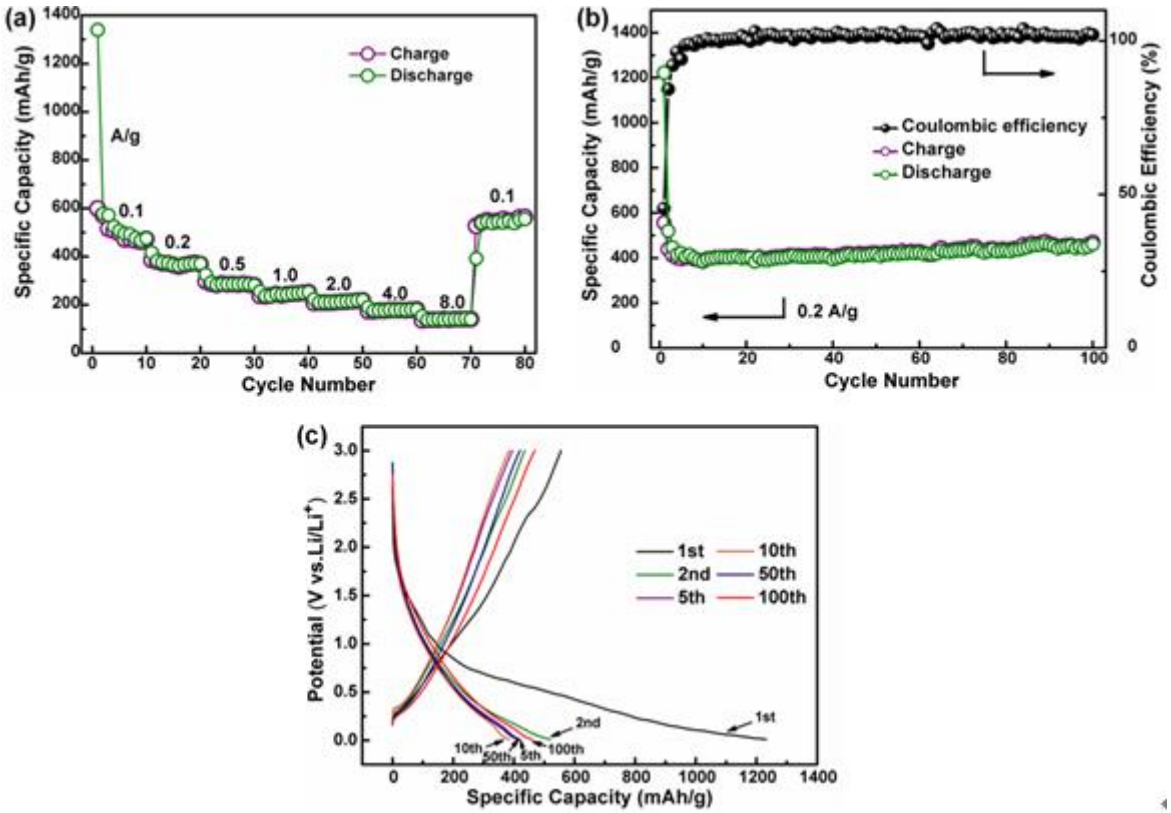

Figure S9. Electrochemical performance of N-GF: a) Rate capability at current rate ranging from 0.1 to 8.0 A g^{-1}; b) Cycling capacity at 0.2 A g^{-1} for 100 cycles with corresponding Coulombic efficiency. Notably, the N-GF only delivers an initial Coulombic efficiency as low as 45.3%. (c) Typical galvanostatic charge-discharge profiles of N-GF at 0.2 A g^{-1} for different cycles. From the charge/discharge profiles, it can be seen that there are no discharge and charge plateaus, indicative of a good electrochemical stability in the chosen electrochemical potential range (0.01-3.0 V).

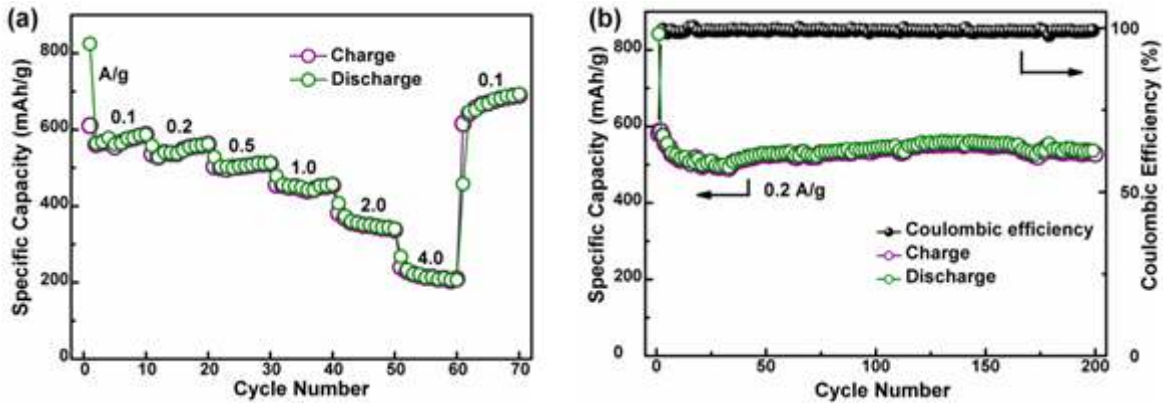

Figure S10. Electrochemical performance of bare MnO@N-GSC/GR in the absence of carbon black: a) Rate capability at current rate ranging from 0.1 to 4.0 A g^{-1}; b) Cycling performance at 0.2 A g^{-1} for 200 cycles. Although there is a decline in the electrochemical performance of the carbon black-free MnO@N-GSC/GR electrode as compared to the electrode with carbon black, it still competitive to that of MnO/G and MnO_2 NWs electrodes (with the addition of carbon black). Hence, it can be expected that the conductive agent can be reduced or even avoided for fabricating electrodes with our prepared GSC-modified MnO.

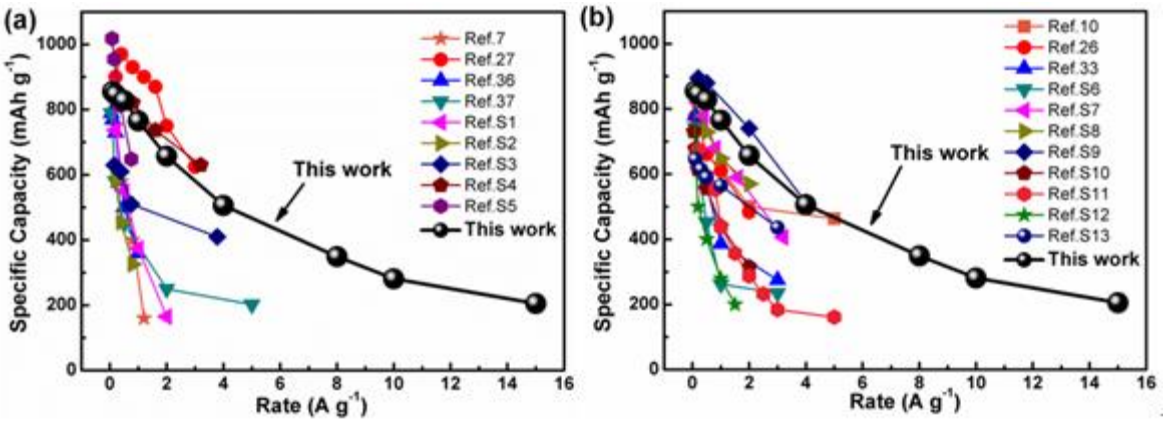

Figure S11. Comparison of the rate capability of MnO@N-GSC/GR with previously reported a) graphene- and b) amorphous carbon-modified MnO composites.

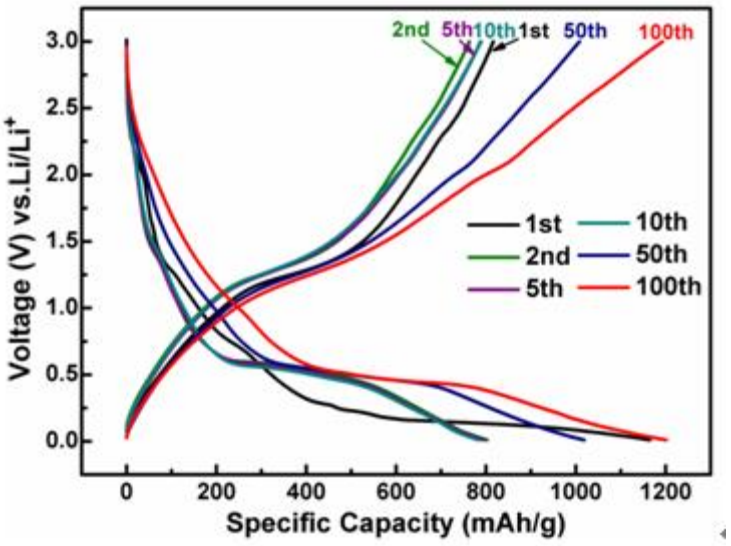

Figure S12. Galvanostatic charge/discharge profiles of MnO@N-GSC/GR at 0.2 A g^{-1} for different cycles.

Table S1. Comparison of the cycling performance of previously reported MnO-based anode materials with our work

MnO-based materials	Current density ($A\ g^{-1}$)	Cycle number (Times)	Reversible capacity ($mAh\ g^{-1}$)	Ref.
MnO particles/graphene	0.1	85	900	[7]
MnO nanocrystals/graphene	2.0	400	843	[27]
MnO nanowires/graphene	0.5	500	930	[36]
MnO/N-doped graphene	0.1	90	772	[37]
MnO@C/graphene	0.1	350	754	[S1]
MnO nanoparticles/graphene	0.1	50	665	[S2]
MnO-attached graphene sheets	0.1	90	772	[S3]
Graphene-coated MnO	0.8	60	680	[S4]
Graphene-loaded MnO nanospheres	0.15	50	846	[S5]
MnO/C nanopeapods	2.0	1000	525	[10]
MnO/C core-shell nanowires	0.1	100	903	[26]
Carbon-loaded MnO nanoparticles	0.1	100	952	[33]
Hollow MnO/C microspheres	0.1	50	700	[S6]
3D porous MnO/C microspheres	0.8	100	800	[S7]
Coaxial MnO/N-doped carbon nanorods	0.5	100	982	[S8]
MnO/C yolk-shell spheres	0.2	500	1040	[S9]
Ultralong MnO/C coaxial nanowires	1.0	600	480	[S10]
MnO dispersed in carbon spheres	0.5	300	501	[S11]
MnO@C/N-doped carbon webs	1.0	700	1268	[S12]
Hollow porous MnO/C composites	0.1	50	730	[S13]
MnO/carbon microsheets	0.1	50	797	[S14]
MnO/carbon nanofibers	1.0	200	575	[S15]
3D hierarchical MnO/N-GSC/GR heterostructure	**2.0**	**1000**	**812**	**This work**

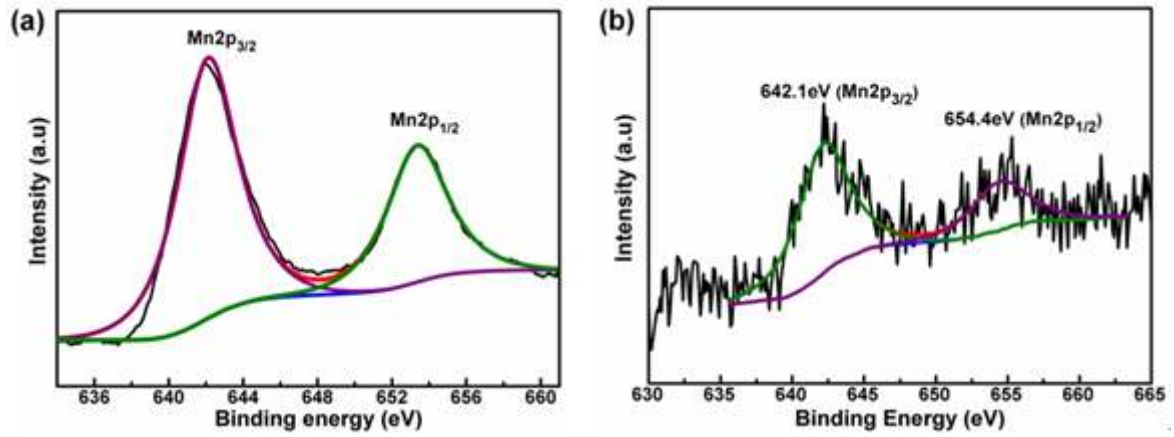

Figure S13. High-resolution Mn 2p XPS spectra of the MnO@N-GSC/GR electrode a) before and b) after 100 cycles at 0.2 A g^{-1}. As shown in Figure S12a, two peaks at 653.3 eV and 641.8 eV can be assigned to Mn(II) $2p_{1/2}$ and $2p_{3/2}$, respectively, confirming the existence of Mn^{2+} in MnO. After 100 cycles, the XPS spectrum (Figure S12b) reveals that the Mn 2p peaks become broader and weaker, in which the two peaks for Mn $2p_{1/2}$ and $2p_{3/2}$ have been shifted at about 654.4 and 642.1 eV, respectively, characteristic of Mn^{4+}, verifying that the Mn^{2+} ions in MnO can be re-oxidized to a higher oxidation state.

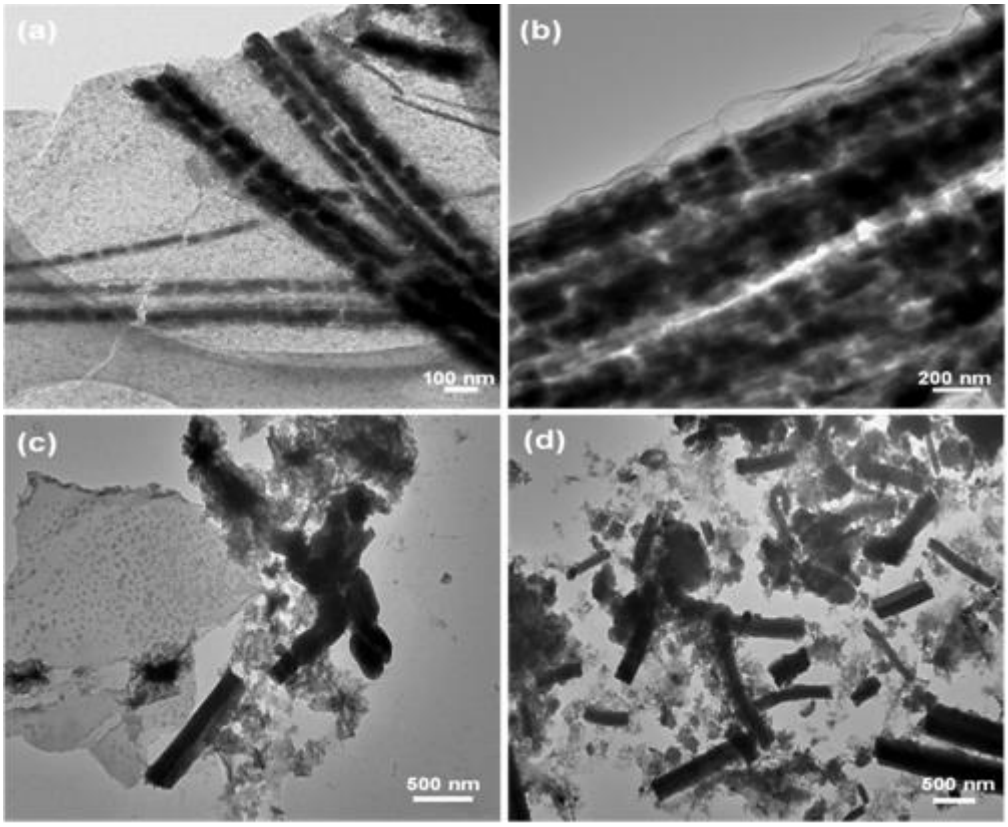

Figure S14. a,b) TEM images of the MnO@N-GSC/GR after 1000 deep cycles at current density of 2.0 A g^{-1}. c,d) TEM images of (c) MnO/G and (d) MnO_2 NWs after only 100 cycles at current density of 0.2 A g^{-1}.

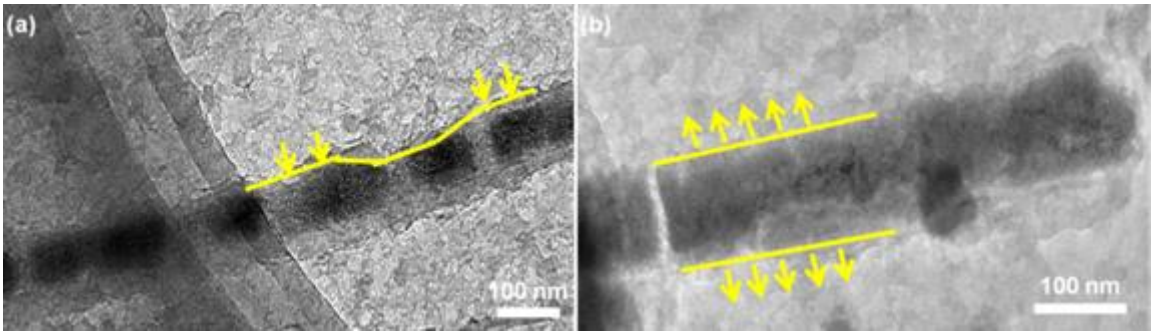

Figure S15. TEM images of the MnO@N-GSC/GR after the 1000th cycle a) charging (delithiation state) and b) discharging (lithiation state).

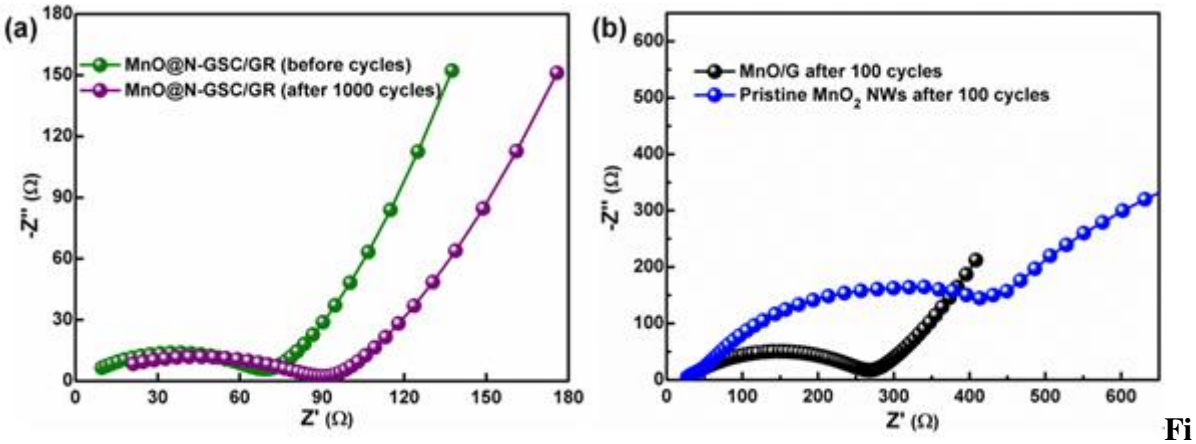

Figure S16. EIS results of a) MnO@N-GSC/GR before and after 1000 cycles, and b) MnO/G and MnO_2 NWs after 100 cycles.

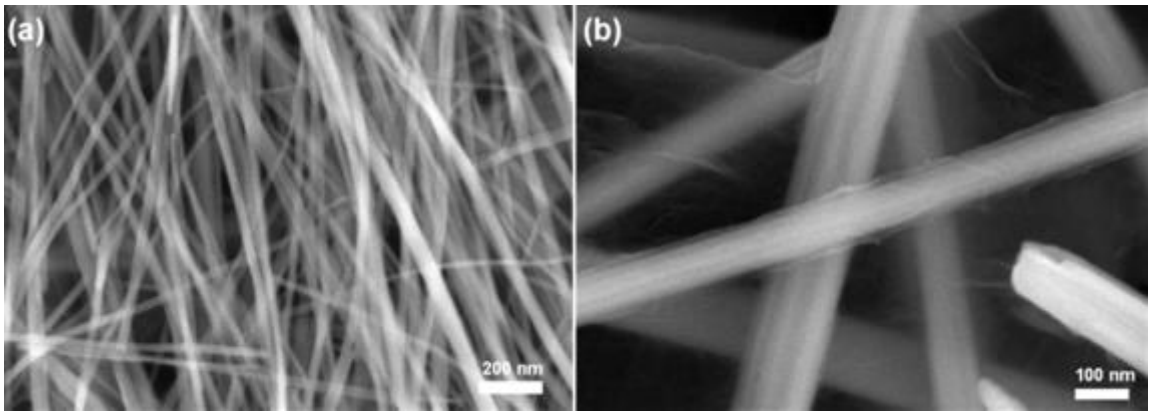

Figure S17. The extension of the preparation method to the synthesis of GSC/V_2O_5-based electrochemically active materials: a) FESEM image of pristine 1D V_2O_5 nanowires; b) FESEM image of the resultant product by treating the V_2O_5 nanowires through the same preparation method, revealing that the vanadium oxide component can be wrapped with graphene scroll to form 1D core-sheath coaxial nanocables whilst embedded in a cross-linked network of graphene ribbon. Hence, this strategy proposed in our study holds great promise for developing high performance TMO_x-based electrode materials.

Reference

[1] Y. H. Wang, X. Ding, F. Wang, J. Q. Li, S. Y. Song, H. J. Zhang, Chem. Sci. **2016**, **DOI:** 10.1039/c5sc04668h.

[2] Y. J. Mai, D. Zhang, Y. Q. Qiao, C. D. Gu, X. L. Wang, J. P. Tu, *J. Power Sources*. **2012**, *216*, 201.

[3] C. T. Hsieh, C. Y. Lin, J. Y. Lin, *Electrochimica Acta* **2011**, *56*, 8861.

[4] B. K. Zou, Y. Y. Zhang, J. Y. Wang, X. Liang, X. H. Ma, C. H. Chen, *Electrochimica Acta* **2015**, *167*, 25.

[5] X. Y. Jiang, X. M. Zhu, X. L. Liu, L. F. Xiao, X. P. Ai, H. X. Yang, Y. L. Cao, *Electrochimica Acta* **2016**, *196*, 431.

[6] Y. Xia, Z. Xiao, X. Dou, H. Huang, X. Lu, R. Yan, Y. Gan, *ACS Nano* **2013**, *7*, 7083.

[7] K. Su, C. Wang, H. G. Nie, Y. Guan, F. Liu, J. T. Chen, *J. Mater. Chem. A* **2014**, *2*, 10000.

[8] X. Gu, J. Yue, L. Chen, S. Liu, H. Y. Xu, J. Yang, Y. T. Qian, X. B. Zhao, *J. Mater. Chem. A* **2015**, *3*, 1037.

[9] S. B. Wang, C. L. Xiao, Y. L. Xing, H. Z. Xu, S. C. Zhang, *J. Mater. Chem. A* **2015**, *3*, 15591.

[10] J. G. Wang, C. B. Zhang, D. D. Jin, K. Y. Xie, B. Q. Wei, *J. Mater. Chem. A* **2015**, *3*, 13699.

[11] H. Hu, H. Y. Cheng, Z. F. Liu, Y. Yu, *Electrochimica Acta* **2015**, *152*, 44.

[12] W. M. Chen, L. Qie, Y. Shen, Y. M. Sun, L. X. Yuan, X. L. Hu, W. X. Zhang, Y. H. Huang, *Nano Energy* **2013**, *2*, 412.

[13] W. J. Zhu, H. Huang, W. K. Zhang, X. Y. Tao, Y. P. Gan, Y. Xia, H. Yang, X. Z. Guo, *Electrochimica Acta* **2015**, *152*, 286.

[14] J. L. Liu, N. Chen, Q. M. Pan, *J. Power Sources*. **2015**, *299,* 265.

[15] B. Liu, X. L. Hu, H. H. Xu, W. Luo, Y. M. Sun, Y. H. Huang, *Sci. Rep.* **2014**, *4*, 4299.

[16] B. Lan, L. Yu, T. Lin, G. Cheng, M. Sun, F. Ye, Q. Sun, J. He, *ACS Appl. Mater. Interfaces* **2013**, *5*, 7458.